PAPER • OPEN ACCESS

High-temperature superconductivity in the two-dimensional *t*–*J* model: Gutzwiller wavefunction solution

To cite this article: Jan Kaczmarczyk *et al* 2014 *New J. Phys.* **16** 073018

New Journal of Physics
The open access journal at the forefront of physics
Deutsche Physikalische Gesellschaft DPG | IOP Institute of Physics

High-temperature superconductivity in the two-dimensional *t–J* model: Gutzwiller wavefunction solution

Jan Kaczmarczyk[1], Jörg Bünemann[2] and Józef Spałek[1,3]

[1] Instytut Fizyki im. Mariana Smoluchowskiego, Uniwersytet Jagielloński, Reymonta 4, 30-059 Kraków, Poland
[2] Institut für Theoretische Physik, Leibniz Universität, D-30167 Hannover, Germany
[3] Akademickie Centrum Materiałów i Nanotechnologii (ACMiN), AGH, Al. Mickiewicza 30, 30-059 Kraków, Poland
E-mail: jan.kaczmarczyk@uj.edu.pl, buenemann@googlemail.com and ufspalek@if.uj.edu.pl

Received 20 January 2014, revised 24 April 2014
Accepted for publication 8 May 2014
Published 14 July 2014

New Journal of Physics **16** (2014) 073018
doi:10.1088/1367-2630/16/7/073018

Abstract

A systematic diagrammatic expansion for Gutzwiller wavefunctions (DE-GWFs) proposed very recently is used for the description of the superconducting (SC) ground state in the two-dimensional square-lattice *t–J* model with the hopping electron amplitudes t (and t') between nearest (and next-nearest) neighbors. For the example of the SC state analysis we provide a detailed comparison of the method's results with those of other approaches. Namely, (i) the truncated DE-GWF method reproduces the variational Monte Carlo (VMC) results and (ii) in the lowest (zeroth) order of the expansion the method can reproduce the analytical results of the standard Gutzwiller approximation (GA), as well as of the recently proposed 'grand-canonical Gutzwiller approximation' (called either GCGA or SGA). We obtain important features of the SC state. First, the SC gap at the Fermi surface resembles a $d_{x^2-y^2}$ wave only for optimally and overdoped systems, being diminished in the antinodal regions for the underdoped case in a qualitative agreement with experiment. Corrections to the gap structure are shown to arise from the longer range of the real-space pairing. Second, the nodal Fermi velocity is almost constant as a function of doping and agrees semi-quantitatively with experimental results. Third, we compare the

doping dependence of the gap magnitude with experimental data. Fourth, we analyze the **k**-space properties of the model: Fermi surface topology and effective dispersion. The DE-GWF method opens up new perspectives for studying strongly correlated systems, as it (i) works in the thermodynamic limit, (ii) is comparable in accuracy to VMC, and (iii) has numerical complexity comparable to that of the GA (i.e., it provides the results much faster than the VMC approach).

Keywords: t–J model, high-temperature superconductivity, Gutzwiller wave function, unconventional superconductivity, variational Monte–Carlo method

1. Introduction

The Hubbard and the t–J models of strongly correlated fermions play an eminent role in rationalizing the principal properties of high-temperature superconductors (for recent reviews see [2, 10, 37, 47, 53]). The relative role of the particles' correlated motion and the binding provided by the kinetic exchange interaction can be clearly visualized in the effective t–J model, where the effective hopping energy $\sim|t|\delta \sim (0.35\ \mathrm{eV})\delta$ ($\delta \equiv 1 - 2n$ is the hole doping) is comparable to or even lower than the kinetic exchange integral $J \approx 0.12$ eV. Simply put, the hopping electron drags behind its exchange-coupled nearest neighbor (n.n.) via empty sites and thus preserves the locally bound configuration in such correlated motion throughout the lattice [56]. In effect, this real-space pairing picture is complementary to the more standard virtual boson (paramagnon) exchange mechanism, which involves, explicitly or implicitly, a quasiparticle picture and concomitant with it reciprocal-space language [21, 36, 39, 45]. Unfortunately, no single unifying approach, if possible at all, exists in the literature which would unify the Eliashberg-type and the real-space approaches, out of which a Cooper-pair condensate would emerge as a universal state for arbitrary ratio of the band energy $\sim W$ to the Coulomb repulsion U. This exclusive character of the approaches is ascribed to the presence of the Mott–Hubbard phase transition that takes place for $W/U \approx 1$ (appearing for the half-filled band case), which also delineates the physics in the strong-correlation limit for a doped-Mott metallic state, for W substantially smaller than U. This is the regime where the t–J model is assumed to be valid, even in the presence of partially filled oxygen $2p$ states [3, 21, 58, 73]. The validity of this type of physics is assumed throughout the present paper, and a quantitative analysis of selected experimental properties, as well as a comparison with variational Monte Carlo (VMC) results, is undertaken.

One of the approaches designed to interpolate between the $W/U \gg 1$ and $W/U \lesssim 1$ limits is the Gutzwiller wavefunction (GWF) approach [19]. Unfortunately, the method does not allow for an extrapolation to the $W/U \ll 1$ limit starting from the Hubbard model, at least in the simpler Gutzwiller approximation (GA) [72]. Therefore, different forms of GA-like approaches, appropriate for the t–J model, have been invented under the name of renormalized mean field theory (RMFT) [10, 15, 16, 26, 34, 46, 63, 72]. The last approach based on the t–J model provides a rationalization of the principal characteristics of high temperature superconductors, including selected properties in a semiquantitative manner, particularly when the so-called statistically consistent Gutzwiller approach (SGA) [1, 23, 25, 26, 29, 30, 57, 64, 70, 71] is

incorporated into RMFT. However, one should also mention that neither GA nor SGA provides a stable superconducting state in the Hubbard model.

Under these circumstances, we have undertaken a project involving a full GWF solution for the Hubbard model by developing a systematic diagrammatic expansion of the GWF (DE-GWF), which becomes applicable to two- and higher-dimensional systems, for both normal [5] and superconducting [28] states. Earlier, this solution was carried through in one spatial dimension in an iterative manner [35, 44]. Obviously, the DE-GWF should reduce to SGA in the limit of infinite dimensions. Here, a detailed analysis is provided for the *t*–*J* model, together with a detailed comparison to experiment, as well as to the VMC and GA results. The limitations of the present approach are also discussed, particularly the inability to describe the pseudogap appearance.

The structure of the paper is as follows. In section 2 we present the DE-GWF method (cf also appendices A and B). In sections 3 and 4 (cf also appendices C, D and E) we provide details of the numerical analysis and discuss physical results, respectively. In the latter section, we also compare our results with experiment and relate them to VMC and GA results. Finally, in section 5 we draw conclusions and overview our approach.

2. The method

2.1. *t*–*J* model

We start with the *t*–*J* model Hamiltonian[4] on a two-dimensional, infinite square lattice

$$\hat{H} = \hat{H}_0 + \hat{H}_{ex}, \tag{1}$$

$$\hat{H}_0 = \sum_{\mathbf{i},\mathbf{j},\sigma} t_{\mathbf{ij}} \hat{c}^{\dagger}_{\mathbf{i},\sigma} \left(1 - \hat{n}_{\mathbf{i}\bar{\sigma}}\right) \hat{c}_{\mathbf{j},\sigma} \left(1 - \hat{n}_{\mathbf{j}\bar{\sigma}}\right), \tag{2}$$

$$\hat{H}_{ex} = J \sum_{\langle \mathbf{i},\mathbf{j} \rangle} \left(\hat{S}_{\mathbf{i}} \cdot \hat{S}_{\mathbf{j}} - c \frac{1}{4} \hat{\nu}_{\mathbf{i}} \hat{\nu}_{\mathbf{j}} \right), \tag{3}$$

where the projected operators are $\hat{\nu}_{\mathbf{i}} = \hat{\nu}_{\mathbf{i}\uparrow} + \hat{\nu}_{\mathbf{i}\downarrow}$ with $\hat{\nu}_{\mathbf{i}\sigma} \equiv \hat{n}_{\mathbf{i}\sigma}\left(1 - \hat{n}_{\mathbf{i}\bar{\sigma}}\right)$, the first term is the kinetic energy part and the second expresses the full form of the kinetic exchange (with $c \equiv 1$). The spin operator is defined as $\hat{S}_{\mathbf{i}} = \left\{ \hat{S}^{z}_{\mathbf{i}}, \hat{S}^{+}_{\mathbf{i}}, \hat{S}^{-}_{\mathbf{i}} \right\} \equiv \left(1/2 \left(\hat{n}_{\mathbf{i},\uparrow} - \hat{n}_{\mathbf{i},\downarrow} \right), \hat{c}^{\dagger}_{\mathbf{i},\uparrow} \hat{c}_{\mathbf{i},\downarrow}, \hat{c}^{\dagger}_{\mathbf{i},\downarrow} \hat{c}_{\mathbf{i},\uparrow} \right)$ and $\sum_{\langle \mathbf{i},\mathbf{j} \rangle}$ denotes summation over pairs of n.n. sites (bonds). The parameter c is used to switch on ($c = 1$) or off ($c = 0$) the density–density interaction term reproducing the two forms of the model used in the literature. Unless stated otherwise, the system's spin isotropy and the translational invariance are not assumed and the analytical results presented in this section are valid for phases with broken symmetries. We study system properties in the thermodynamic limit; i.e., the system size L is infinite. We also neglect the three-site terms[4]. Note also that the fermionic representation of the spin operator is identical in both the starting $\left(\hat{c}^{\dagger}_{\mathbf{i},\sigma}, \hat{c}_{\mathbf{i},\sigma} \right)$ and the projected $\left(\hat{c}^{\dagger}_{\mathbf{i},\sigma} \left(1 - \hat{n}_{\mathbf{i}\bar{\sigma}}\right) \right)$, $\left(\hat{c}_{\mathbf{i},\sigma} \left(1 - \hat{n}_{\mathbf{i}\bar{\sigma}}\right) \right)$ representations.

[4] For the original derivation of the *t*–*J* model from the Hubbard model see [77, 78]. For didactical exposition see [79].

2.2. Trial wavefunction

The principal task within a Gutzwiller-type [19] approach is the calculation of the expectation value of the starting Hamiltonian with respect to the trial wavefunction, which is defined as

$$\left|\Psi_{\mathrm{G}}\right\rangle = \hat{P}\ \left|\Psi_0\right\rangle \equiv \prod\nolimits_{\mathbf{i}} \hat{P}_{\mathbf{i}}\ \left|\Psi_0\right\rangle\ , \tag{4}$$

where $\left|\Psi_0\right\rangle$ is a single-particle product state (Slater determinant) to be specified later. We define the local Gutzwiller correlator in the atomic basis of the form

$$\hat{P}_{\mathbf{i}} \equiv \sum_{\Gamma} \lambda_{\mathbf{i},\Gamma}\ \left|\Gamma\right\rangle_{\mathbf{i}\,\mathbf{i}}\left\langle\Gamma\right|\ , \tag{5}$$

with variational parameters $\lambda_{\mathbf{i},\Gamma} \in \left\{\lambda_{\mathbf{i},\varnothing}, \lambda_{\mathbf{i},1\uparrow}, \lambda_{\mathbf{i},1\downarrow}, \lambda_{\mathbf{i},d}\right\}$, which describe the occupation probabilities of the four possible local states $\left\{\left|\Gamma\right\rangle_{\mathbf{i}}\right\} \equiv \left\{\left|\varnothing\right\rangle_{\mathbf{i}}, \left|\uparrow\right\rangle_{\mathbf{i}}, \left|\downarrow\right\rangle_{\mathbf{i}}, \left|\uparrow\downarrow\right\rangle_{\mathbf{i}}\right\}$. A particularly useful choice of the parameters $\lambda_{\mathbf{i},\Gamma}$ is the one which obeys

$$\hat{P}_{\mathbf{i}}^{2} \equiv 1 + x\hat{d}_{\mathbf{i}}^{\mathrm{HF}}, \tag{6}$$

where the Hartree–Fock operators are defined by $\hat{d}_{\mathbf{i}}^{\mathrm{HF}} \equiv \hat{n}_{\mathbf{i}\uparrow}^{\mathrm{HF}}\hat{n}_{\mathbf{i}\downarrow}^{\mathrm{HF}}$ and $\hat{n}_{\mathbf{i}\sigma}^{\mathrm{HF}} \equiv \hat{n}_{\mathbf{i},\sigma} - n_{\mathbf{i}\sigma}$ with $n_{\mathbf{i}\sigma} = \left\langle\Psi_0\right|\hat{n}_{\mathbf{i}\sigma}\left|\Psi_0\right\rangle$. This form of $\hat{P}_{\mathbf{i}}^{2}$ decisively simplifies the calculations by eliminating the so-called 'Hartree bubbles' [5, 18].

For the t–J model, we work with zero double-occupancy, which sets $\lambda_{\mathbf{i},d} = 0$ and eliminates x as a variational parameter from the solution procedure. Explicitly, from the conditions in equations (5) and (6) we find $\lambda_{\mathbf{i},d}^{2} = 1 + x\left(1 - n_{\mathbf{i}\uparrow}\right)\left(1 - n_{\mathbf{i}\downarrow}\right) = 0$. Calculating x and inserting into the expressions for $\lambda_{\mathbf{i},1\sigma}$ and $\lambda_{\mathbf{i},\varnothing}$ gives

$$\lambda_{\mathbf{i},1\sigma} = \frac{1}{\sqrt{1 - n_{\mathbf{i}\bar{\sigma}}}}, \tag{7}$$

$$\lambda_{\mathbf{i},\varnothing} = \sqrt{\frac{1 - n_{\mathbf{i}}}{\left(1 - n_{\mathbf{i}\sigma}\right)\left(1 - n_{\mathbf{i}\bar{\sigma}}\right)}}, \tag{8}$$

where $n_{\mathbf{i}} = n_{\mathbf{i}\uparrow} + n_{\mathbf{i}\downarrow}$.

2.3. Diagrammatic sums

Here we discuss the analytical procedure of calculating the expectation value

$$W \equiv \left\langle\hat{H}\right\rangle_{\mathrm{G}} \equiv \frac{\left\langle\Psi_{\mathrm{G}}\right|\hat{H}\left|\Psi_{\mathrm{G}}\right\rangle}{\left\langle\Psi_{\mathrm{G}}\middle|\Psi_{\mathrm{G}}\right\rangle} \equiv \frac{\left\langle\Psi_0\right|\hat{P}\hat{H}\hat{P}\left|\Psi_0\right\rangle}{\left\langle\Psi_0\right|\hat{P}^{2}\left|\Psi_0\right\rangle} \tag{9}$$

in detail for the kinetic-energy term, and we summarize the results for other terms. We start with expressions for the relevant expectation values of interest via the power series in x, i.e.,

$$\left\langle \Psi_{\mathrm{G}} \middle| \Psi_{\mathrm{G}} \right\rangle = \left\langle \prod_{\mathbf{l}} \hat{P}_{\mathbf{l}}^{2} \right\rangle_{0} = \sum_{k=0}^{\infty} \frac{x^{k}}{k!} \sum_{\mathbf{l}_{1},\ldots,\mathbf{l}_{k}}{}' \left\langle \hat{d}^{\mathrm{HF}}_{\mathbf{l}_{1},\ldots,\mathbf{l}_{k}} \right\rangle_{0}, \tag{10}$$

$$\left\langle \Psi_{\mathrm{G}} \right| \hat{c}^{\dagger}_{\mathbf{i},\sigma} \hat{c}_{\mathbf{j},\sigma} \left| \Psi_{\mathrm{G}} \right\rangle = \left\langle \tilde{c}^{\dagger}_{\mathbf{i},\sigma} \tilde{c}_{\mathbf{j},\sigma} \prod_{\mathbf{l}(\neq \mathbf{i},\mathbf{j})} \hat{P}_{\mathbf{l}}^{2} \right\rangle_{0} = \sum_{k=0}^{\infty} \frac{x^{k}}{k!} \sum_{\mathbf{l}_{1},\ldots,\mathbf{l}_{k}}{}' \left\langle \tilde{c}^{\dagger}_{\mathbf{i},\sigma} \tilde{c}_{\mathbf{j},\sigma} \hat{d}^{\mathrm{HF}}_{\mathbf{l}_{1},\ldots,\mathbf{l}_{k}} \right\rangle_{0}, \tag{11}$$

where $\left\langle (\ldots) \right\rangle_{0} \equiv \left\langle \Psi_{0} \right| (\ldots) \left| \Psi_{0} \right\rangle$, $\tilde{c}^{(\dagger)}_{\mathbf{i},\sigma} \equiv \hat{P}_{\mathbf{i}} \hat{c}^{(\dagger)}_{\mathbf{i},\sigma} \hat{P}_{\mathbf{i}}$, and we have defined $\hat{d}^{\mathrm{HF}}_{\mathbf{l}_{1},\ldots,\mathbf{l}_{k}} \equiv \hat{d}^{\mathrm{HF}}_{\mathbf{l}_{1}} \cdots \hat{d}^{\mathrm{HF}}_{\mathbf{l}_{k}}$ with $\hat{d}^{\mathrm{HF}}_{\varnothing} \equiv 1$, whereas the primed sums have the summation restrictions $\mathbf{l}_{p} \neq \mathbf{l}_{p'}$, $\mathbf{l}_{p} \neq \mathbf{i}, \mathbf{j}$ for all p, p'.

Expectation values can now be evaluated by means of Wick's theorem [14] and are carried out in real space. Then, in the resulting diagrammatic expansion, the kth order terms of equations (10)–(11) correspond to diagrams with one (or two) external vertices on sites $\mathbf{i}$ (or $\mathbf{i}$ and $\mathbf{j}$) and k internal vertices. These vertices are connected with lines (corresponding to contractions from Wick's theorem), which in the case of the superconducting state with intersite pairing are given by

$$P^{\sigma}_{\mathbf{l},\mathbf{l}'} \equiv \left\langle \hat{c}^{\dagger}_{\mathbf{l},\sigma} \hat{c}_{\mathbf{l}',\sigma} \right\rangle_{0} - \delta_{\mathbf{l},\mathbf{l}'} n_{\mathbf{l},\sigma}, \qquad S_{\mathbf{l},\mathbf{l}'} \equiv \left\langle \hat{c}^{\dagger}_{\mathbf{l},\uparrow} \hat{c}^{\dagger}_{\mathbf{l}',\downarrow} \right\rangle_{0}, \tag{12}$$

where $\bar{\uparrow} = \downarrow$, $\bar{\downarrow} = \uparrow$. At this point, the application of the linked-cluster theorem [14] yields [5] the analytical result for the kinetic-energy term

$$\left\langle \hat{H}_{0} \right\rangle_{\mathrm{G}} = \sum_{\mathbf{i},\mathbf{j},\sigma} t_{\mathbf{i},\mathbf{j}} \left(q_{\mathbf{i}\sigma} q_{\mathbf{j}\sigma} T^{(1),(1)}_{\mathbf{i},\mathbf{j},\sigma} + q_{\mathbf{i}\sigma} \alpha_{\mathbf{j}\sigma} T^{(1),(3)}_{\mathbf{i},\mathbf{j},\sigma} + \alpha_{\mathbf{i}\sigma} q_{\mathbf{j}\sigma} T^{(3),(1)}_{\mathbf{i},\mathbf{j},\sigma} + \alpha_{\mathbf{i}\sigma} \alpha_{\mathbf{j}\sigma} T^{(3),(3)}_{\mathbf{i},\mathbf{j},\sigma} \right), \tag{13}$$

where

$$q_{\mathbf{i}\sigma} \equiv \lambda_{\mathbf{i},1\sigma} \lambda_{\mathbf{i},\varnothing} (1 - n_{\mathbf{i}}) = \sqrt{\frac{1 - n_{\mathbf{i}}}{1 - n_{\mathbf{i},\sigma}}}, \tag{14}$$

$$\alpha_{\mathbf{i}\sigma} \equiv -\lambda_{\mathbf{i},1\sigma} \lambda_{\mathbf{i},\varnothing} = -\frac{1}{1 - n_{\mathbf{i}\bar{\sigma}}} \sqrt{\frac{1 - n_{\mathbf{i}}}{1 - n_{\mathbf{i},\sigma}}} = -\frac{q_{\mathbf{i}\sigma}}{1 - n_{\mathbf{i}\bar{\sigma}}}. \tag{15}$$

The diagrammatic sums appearing in equation (13) are defined by

$$S = \sum_{k=0}^{\infty} \frac{x^{k}}{k!} S(k), \tag{16}$$

where

$$S \in \left\{ T^{(1),(1)}_{\mathbf{i},\mathbf{j},\sigma}, T^{(1),(3)}_{\mathbf{i},\mathbf{j},\sigma}, T^{(3),(1)}_{\mathbf{i},\mathbf{j},\sigma}, T^{(3),(3)}_{\mathbf{i},\mathbf{j},\sigma} \right\} \tag{17}$$

and the kth order sum contributions have the following forms:

$$T^{(1)[(3)],(1)[(3)]}_{\mathbf{i},\mathbf{j},\sigma}(k) \equiv \sum_{\mathbf{l}_{1},\ldots,\mathbf{l}_{k}} \left\langle \left[\hat{n}^{\mathrm{HF}}_{\mathbf{i},\bar{\sigma}} \right] \hat{c}^{\dagger}_{\mathbf{i},\sigma} \left[\hat{n}^{\mathrm{HF}}_{\mathbf{j},\bar{\sigma}} \right] \hat{c}_{\mathbf{j},\sigma} \hat{d}^{\mathrm{HF}}_{\mathbf{l}_{1},\ldots,\mathbf{l}_{k}} \right\rangle^{\mathrm{c}}_{0} \tag{18}$$

where $\left\langle \ldots \right\rangle^{\mathrm{c}}_{0}$ indicates that only the connected diagrams are to be retained (see appendix A for exemplary diagrams and their contributions to diagrammatic sums in the two lowest orders). The notation $(1)\left[(3)\right]$ means that for the index (3) the term in square brackets also needs to be

taken into account, e.g. $T^{(1),(3)}_{\mathbf{i},\mathbf{j},\sigma}(k) \equiv \sum_{\mathbf{l}_1,\ldots,\mathbf{l}_k} \left\langle \hat{c}^{\dagger}_{\mathbf{i},\sigma} \hat{n}^{\mathrm{HF}}_{\mathbf{j},\bar{\sigma}} \hat{c}_{\mathbf{j},\sigma} \hat{d}^{\mathrm{HF}}_{\mathbf{l}_1,\ldots,\mathbf{l}_k} \right\rangle^{\mathrm{c}}_0$. In the following expressions we will drop the brackets in the upper indices of diagrammatic sums for the sake of brevity.

The exchange term can be rewritten in the form

$$J \sum_{\langle \mathbf{i},\mathbf{j} \rangle} \left(\hat{S}_{\mathbf{i}} \hat{S}_{\mathbf{j}} - \frac{\mathbf{1}}{\mathbf{4}} \hat{\nu}_{\mathbf{i}} \hat{\nu}_{\mathbf{j}} \right) = J \sum_{\langle \mathbf{i},\mathbf{j} \rangle} \left(\frac{\hat{S}^{+}_{\mathbf{i}} \hat{S}^{-}_{\mathbf{j}} + \hat{S}^{-}_{\mathbf{i}} \hat{S}^{+}_{\mathbf{j}}}{2} + \hat{S}^{z}_{\mathbf{i}} \hat{S}^{z}_{\mathbf{j}} - \frac{1}{4} \hat{\nu}_{\mathbf{i}} \hat{\nu}_{\mathbf{j}} \right), \tag{19}$$

where the spin-component operators are given by $\left\{ \hat{S}^{+}_{\mathbf{i}}, \hat{S}^{-}_{\mathbf{i}}, \hat{S}^{z}_{\mathbf{i}} \right\} = \left\{ \hat{c}^{\dagger}_{\mathbf{i}\uparrow} \hat{c}_{\mathbf{i}\downarrow}, \hat{c}^{\dagger}_{\mathbf{i}\downarrow} \hat{c}_{\mathbf{i}\uparrow}, \frac{1}{2} \left(\hat{n}_{\mathbf{i}\uparrow} - \hat{n}_{\mathbf{i}\downarrow} \right) \right\}$. The expectation values of the exchange term components can be expressed as

$$\frac{1}{2} \left\langle \hat{S}^{+}_{\mathbf{i}} \hat{S}^{-}_{\mathbf{j}} + \hat{S}^{-}_{\mathbf{i}} \hat{S}^{+}_{\mathbf{j}} \right\rangle_{G} = \left[\left(n_{\mathbf{i}\downarrow} - 1 \right) \left(n_{\mathbf{i}\uparrow} - 1 \right) \left(n_{\mathbf{j}\downarrow} - 1 \right) \left(n_{\mathbf{j}\uparrow} - 1 \right) \right]^{-1/2} \frac{S^{22}_{\mathbf{i}\uparrow,\mathbf{j}\downarrow} + S^{22}_{\mathbf{i}\downarrow,\mathbf{j}\uparrow}}{2}. \tag{20}$$

For the expressions of the other components see appendix B.

The diagrammatic sums appearing in the above expressions are defined by equation (16) with

$$S \in \left\{ I^{2}_{\mathbf{i}\sigma}, I^{4}_{\mathbf{i}}, I^{22}_{\mathbf{i}\sigma,\mathbf{j}\sigma'}, I^{24}_{\mathbf{i}\sigma,\mathbf{j}}, I^{42}_{\mathbf{i},\mathbf{j}\sigma}, I^{44}_{\mathbf{i},\mathbf{j}}, S^{22}_{\mathbf{i}\sigma,\mathbf{j}\bar{\sigma}} \right\} \tag{21}$$

and the kth order sum contributions of the following forms:

$$I^{2}_{\mathbf{i}\sigma}(k) \equiv \sum_{\mathbf{l}_1,\ldots,\mathbf{l}_k} \left\langle \hat{n}^{\mathrm{HF}}_{\mathbf{i}\sigma} \hat{d}^{\mathrm{HF}}_{\mathbf{l}_1,\ldots,\mathbf{l}_k} \right\rangle^{\mathrm{c}}_0, \tag{22}$$

$$I^{4}_{\mathbf{i}}(k) \equiv \sum_{\mathbf{l}_1,\ldots,\mathbf{l}_k} \left\langle \hat{d}^{\mathrm{HF}}_{\mathbf{i}} \hat{d}^{\mathrm{HF}}_{\mathbf{l}_1,\ldots,\mathbf{l}_k} \right\rangle^{\mathrm{c}}_0, \tag{23}$$

$$I^{22}_{\mathbf{i}\sigma,\mathbf{j}\sigma'}(k) \equiv \sum_{\mathbf{l}_1,\ldots,\mathbf{l}_k} \left\langle \hat{n}^{\mathrm{HF}}_{\mathbf{i}\sigma} \hat{n}^{\mathrm{HF}}_{\mathbf{j}\sigma'} \hat{d}^{\mathrm{HF}}_{\mathbf{l}_1,\ldots,\mathbf{l}_k} \right\rangle^{\mathrm{c}}_0, \tag{24}$$

$$I^{24}_{\mathbf{i}\sigma,\mathbf{j}}(k) \equiv \sum_{\mathbf{l}_1,\ldots,\mathbf{l}_k} \left\langle \hat{n}^{\mathrm{HF}}_{\mathbf{i}\sigma} \hat{d}^{\mathrm{HF}}_{\mathbf{j}} \hat{d}^{\mathrm{HF}}_{\mathbf{l}_1,\ldots,\mathbf{l}_k} \right\rangle^{\mathrm{c}}_0, \tag{25}$$

$$I^{42}_{\mathbf{i},\mathbf{j}\sigma}(k) \equiv \sum_{\mathbf{l}_1,\ldots,\mathbf{l}_k} \left\langle \hat{d}^{\mathrm{HF}}_{\mathbf{i}} \hat{n}^{\mathrm{HF}}_{\mathbf{j}\sigma} \hat{d}^{\mathrm{HF}}_{\mathbf{l}_1,\ldots,\mathbf{l}_k} \right\rangle^{\mathrm{c}}_0, \tag{26}$$

$$I^{44}_{\mathbf{i},\mathbf{j}}(k) \equiv \sum_{\mathbf{l}_1,\ldots,\mathbf{l}_k} \left\langle \hat{d}^{\mathrm{HF}}_{\mathbf{i}} \hat{d}^{\mathrm{HF}}_{\mathbf{j}} \hat{d}^{\mathrm{HF}}_{\mathbf{l}_1,\ldots,\mathbf{l}_k} \right\rangle^{\mathrm{c}}_0, \tag{27}$$

$$S^{22}_{\mathbf{i}\sigma,\mathbf{j}\bar{\sigma}}(k) \equiv \sum_{\mathbf{l}_1,\ldots,\mathbf{l}_k} \left\langle \hat{c}^{\dagger}_{\mathbf{i}\sigma} \hat{c}_{\mathbf{i}\bar{\sigma}} \hat{c}^{\dagger}_{\mathbf{j}\bar{\sigma}} \hat{c}_{\mathbf{j}\sigma} \hat{d}^{\mathrm{HF}}_{\mathbf{l}_1,\ldots,\mathbf{l}_k} \right\rangle^{\mathrm{c}}_0. \tag{28}$$

In what follows, we evaluate these diagrammatic sums in particular situations.

2.4. Spin-isotropic case

The above expressions simplify significantly when a system with translational invariance and spin isotropy is considered. In general, this situation is applicable when no Néel-type antiferromagnetism occurs, as for the spin-singlet paired state the spin isotropy is preserved.

Explicitly, they become

$$\left\langle \hat{c}^{\dagger}_{\mathbf{i},\sigma}\hat{c}_{\mathbf{j},\sigma}\right\rangle_G = q^2\, T^{11} + 2q\alpha T^{13} + \alpha^2\, T^{33}, \tag{29}$$

$$\frac{1}{2}\left\langle \hat{S}^{+}_{\mathbf{i}}\hat{S}^{-}_{\mathbf{j}} + \hat{S}^{-}_{\mathbf{i}}\hat{S}^{+}_{\mathbf{j}}\right\rangle_G = g_s S^{22}, \tag{30}$$

$$\left\langle \hat{S}^{z}_{\mathbf{i}}\hat{S}^{z}_{\mathbf{j}}\right\rangle_G = g_s\left(\frac{I^{22\uparrow\uparrow} - I^{22\uparrow\downarrow}}{2}\right), \tag{31}$$

$$\begin{aligned}\frac{1}{4}\left\langle \hat{n}_{\mathbf{i}}\hat{n}_{\mathbf{j}}\right\rangle_G = n^2 &+ I^{22\uparrow\uparrow}\frac{(1-2n)^2}{2(n-1)^2} + I^{22\uparrow\downarrow}\frac{(1-2n)^2}{2(n-1)^2} + I^{44}\frac{(1-2n)^2}{(n-1)^4}\\ &+ I^{2}\frac{n(4n-2)}{n-1} + I^{4}\frac{2n(2n-1)}{(n-1)^2} + I^{24}\frac{2(1-2n)^2}{(n-1)^3},\end{aligned} \tag{32}$$

where $n = n_{\mathbf{i}\sigma} = n_{\mathbf{j}\sigma}$, $g_s = \frac{1}{(1-n)^2}$, $q^2 \equiv g_t = (1-2n)/(1-n)$, $\alpha = -q/(1-n)$, and the diagrammatic sums have also been simplified with $I^{22\uparrow\uparrow} = I^{22}_{\mathbf{i}\sigma,\mathbf{j}\sigma}$, $I^{22\uparrow\downarrow} = I^{22}_{\mathbf{i}\sigma,\mathbf{j}\bar{\sigma}}$, $I^{24} = I^{24}_{\mathbf{i}\sigma,\mathbf{j}} = I^{42}_{\mathbf{i},\mathbf{j}\sigma}$, $I^{2} = I^{2}_{\mathbf{i}\sigma} = I^{2}_{\mathbf{j}\sigma}$, and $I^{4} = I^{4}_{\mathbf{i}} = I^{4}_{\mathbf{j}}$, $S^{22} = S^{22}_{\mathbf{i}\sigma,\mathbf{j}\bar{\sigma}}$.

Note that the rotational invariance requires $\left\langle \hat{S}^{z}_{\mathbf{i}}\hat{S}^{z}_{\mathbf{j}}\right\rangle = \left\langle \hat{S}^{x}_{\mathbf{i}}\hat{S}^{x}_{\mathbf{j}}\right\rangle = \left\langle \hat{S}^{y}_{\mathbf{i}}\hat{S}^{y}_{\mathbf{j}}\right\rangle$, which leads to the condition for diagrammatic sums: $S^{22} = I^{22\uparrow\uparrow} - I^{22\uparrow\downarrow}$. We have verified that this condition holds true in our calculations.

2.5. Relation to other approaches

When only the zeroth order of the diagrammatic expansion method is taken into account and under additional simplifications (see below), the analytical results are equivalent to those of the Gutzwiller approximation (GA) [10, 72] and of the recently proposed grand-canonical Gutzwiller approximation (GCGA) [15, 16, 23, 25, 26, 29]. In the zeroth order all the diagrams with unequal degrees of sites **i** and **j** vanish, namely $I^{2}_{\mathbf{i}[\mathbf{j}]\sigma} = I^{4}_{\mathbf{i}[\mathbf{j}]} = I^{24}_{\mathbf{i}\sigma,\mathbf{j}} = I^{42}_{\mathbf{i},\mathbf{j}\sigma} = T^{31}_{\mathbf{i},\mathbf{j},\sigma} = T^{13}_{\mathbf{i},\sigma} = 0$. The remaining diagrammatic sums are given by

$$I^{22}_{\mathbf{i}\sigma\mathbf{j}\sigma} = -P^{2}_{\mathbf{ij}\sigma}, \tag{33}$$

$$I^{22}_{\mathbf{i}\sigma\mathbf{j}\bar{\sigma}} = S^{2}_{\mathbf{ij}}, \tag{34}$$

$$S^{22}_{\mathbf{i}\sigma,\mathbf{j}\bar{\sigma}} = -P_{\mathbf{ij}\uparrow}P_{\mathbf{ij}\downarrow} - S^{2}_{ij}, \tag{35}$$

$$T^{11}_{\mathbf{i},\mathbf{j},\sigma} = P_{\mathbf{ij}\sigma}, \tag{36}$$

$$T^{33}_{\mathbf{i},\mathbf{j},\sigma} = -P_{\mathbf{ij}\sigma}P^{2}_{\mathbf{ij}\bar{\sigma}} - P_{\mathbf{ij}\bar{\sigma}}S^{2}_{ij}. \tag{37}$$

In this situation, and if we additionally disregard the T^{33} and I^{44} terms, relations valid for the isotropic system are obtained:

$$\left\langle \hat{c}^{\dagger}_{\mathbf{i},\sigma}\hat{c}_{\mathbf{j},\sigma}\right\rangle^{(GA)}_{G} = q^{2}\,T^{11} = g_{t}\left\langle \hat{c}^{\dagger}_{\mathbf{i},\sigma}\hat{c}_{\mathbf{j},\sigma}\right\rangle_{0}, \tag{38}$$

$$\left\langle \hat{S}^{+}_{\mathbf{i}}\hat{S}^{-}_{\mathbf{j}} + \hat{S}^{-}_{\mathbf{i}}\hat{S}^{+}_{\mathbf{j}}\right\rangle^{(GA)}_{G} = g_{s}\left\langle \hat{S}^{+}_{\mathbf{i}}\hat{S}^{-}_{\mathbf{j}} + \hat{S}^{-}_{\mathbf{i}}\hat{S}^{+}_{\mathbf{j}}\right\rangle_{0}, \tag{39}$$

$$\left\langle \hat{S}^{z}_{\mathbf{i}}\hat{S}^{z}_{\mathbf{j}}\right\rangle^{(GA)}_{G} = g_{s}\left\langle \hat{S}^{z}_{\mathbf{i}}\hat{S}^{z}_{\mathbf{j}}\right\rangle_{0}, \tag{40}$$

reproducing analytically the results of GA [72]. It is interesting to see how large the difference is between the exact expressions, equations (29)–(32), and their GA approximations, equations (38)–(40). This difference is analyzed in appendix C.

If we consider general phases, and we keep the T^{33} term, then the expressions for the expectation values of the hopping and the exchange term become

$$\left\langle \hat{c}^{\dagger}_{\mathbf{i},\sigma}\hat{c}_{\mathbf{j},\sigma}\right\rangle_{G} = q_{\mathbf{i},\sigma}q_{\mathbf{j},\sigma}\left(P_{\mathbf{ij}\sigma} - P_{\mathbf{ij}\bar{\sigma}}\frac{P_{\mathbf{ij}\sigma}P_{\mathbf{ij}\bar{\sigma}} + S^{2}_{ij}}{\left(1-n_{\mathbf{i}\bar{\sigma}}\right)\left(1-n_{\mathbf{j}\bar{\sigma}}\right)}\right), \tag{41}$$

$$\begin{aligned}\left\langle \hat{S}^{z}_{\mathbf{i}}\hat{S}^{z}_{\mathbf{j}}\right\rangle_{G} = {} & \frac{m_{\mathbf{i}}m_{\mathbf{j}}}{4} + \frac{\left(m_{\mathbf{i}}+1\right)\left(m_{\mathbf{j}}+1\right)\left(-P^{2}_{ij\downarrow}\right)}{4\left(n_{\mathbf{i}\downarrow}-1\right)\left(n_{\mathbf{j}\downarrow}-1\right)} + \frac{\left(-m_{\mathbf{i}}-1\right)\left(1-m_{\mathbf{j}}\right)S^{2}_{\mathbf{ij}}}{4\left(n_{\mathbf{i}\downarrow}-1\right)\left(n_{\mathbf{j}\uparrow}-1\right)} \\ & - \frac{\left(-m_{\mathbf{i}}+1\right)\left(-m_{\mathbf{j}}-1\right)S^{2}_{\mathbf{ij}}}{4\left(n_{\mathbf{i}\uparrow}-1\right)\left(n_{\mathbf{j}\downarrow}-1\right)} + \frac{\left(-m_{\mathbf{i}}+1\right)\left(1-m_{\mathbf{j}}\right)\left(-P^{2}_{ij\uparrow}\right)}{4\left(n_{\mathbf{i}\uparrow}-1\right)\left(n_{\mathbf{j}\uparrow}-1\right)} \\ & + \frac{I^{44}_{\mathbf{ij}}m_{\mathbf{i}}m_{\mathbf{j}}}{\left(n_{\mathbf{i}\downarrow}-1\right)\left(n_{\mathbf{i}\uparrow}-1\right)\left(n_{\mathbf{j}\downarrow}-1\right)\left(n_{\mathbf{j}\uparrow}-1\right)},\end{aligned} \tag{42}$$

$$\frac{1}{2}\left\langle \hat{S}^{+}_{\mathbf{i}}\hat{S}^{-}_{\mathbf{j}} + \hat{S}^{-}_{\mathbf{i}}\hat{S}^{+}_{\mathbf{j}}\right\rangle_{G} = \left[\left(n_{\mathbf{i}\downarrow}-1\right)\left(n_{\mathbf{i}\uparrow}-1\right)\left(n_{\mathbf{j}\downarrow}-1\right)\left(n_{\mathbf{j}\uparrow}-1\right)\right]^{-1/2}\left(-P_{ij\uparrow}P_{ij\downarrow} - S^{2}_{ij\sigma}\right), \tag{43}$$

where $m_{\mathbf{i}} = n_{\mathbf{i}\uparrow} + n_{\mathbf{i}\downarrow}$.

When the four-line contribution from the diagrammatic sum $I^{44}_{\mathbf{ij}}$ (in equation (42)) is neglected, our method reproduces the GCGA results[5]. Explicitly, equations (41), (42), and (43) are equivalent, respectively, to equations (15), (20), and (21) of [15]. In a similar manner, equivalence is obtained for the density–density term, equation (B.1), and the result of the GCGA approach presented in [16] (equation (44) therein). Therefore, within the present approach the results of a sophisticated version of the RMFT [15, 16] are obtained.

2.6. Test case: Gutzwiller wavefunction for one-dimensional t–J model

As a test case of our analytical results we consider the one-dimensional *t–J* model, for which an exact analytical solution has been presented [17] in the paramagnetic case. We calculate the exact value of the spin–spin correlation function $\left\langle \hat{S}^{z}_{\mathbf{i}}\hat{S}^{z}_{\mathbf{j}}\right\rangle$ using equation (49) from [34] and with our DE-GWF method. The difference between these two results is presented in figure 1 as a

[5] For the spin-isotropic case $m_{\mathbf{i}} = m_{\mathbf{j}} = 0$, and the four line contribution to equation (42) vanishes making the zeroth order DE-GWF equivalent to GCGA.

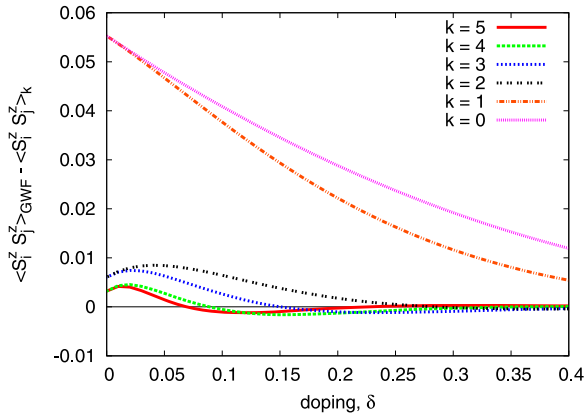

Figure 1. Difference between the exact GWF results for the one-dimensional t–J model and our DE-GWF results as a function of doping for orders $k = 0$–5. The DE-GWF results change most when an even order is taken into account (e.g., inclusion of the fourth order terms gives larger change than inclusion of the third). The largest discrepancy of the results is close to half filling, where the expansion parameter x approaches its maximal absolute value of $|x| = 4$.

function of doping in the orders $k = 0$–5. It can be seen that the fifth-order results are very close to the exact results for the doping $\delta \gtrsim 0.05$. The discrepancy should decrease with increasing dimensionality d, as the zeroth-order results are exact for infinite d. The fifth-order results are more than one order of magnitude closer to the exact values than those obtained in the zeroth order. Note also that the latter ($k = 0$ results) are, for the present spin–spin correlation function, equivalent to those of GCGA [15] and GA [72] approaches.

The order k to which we carry out our expansion is not the only parameter affecting convergence. Another one is the number of $|\Psi_0\rangle$ lines (defined in equation (12)) included when calculating the diagrammatic sums. Its effect on results for the spin–spin correlation function is analyzed in appendix D.

3. Self-consistent variational solution

In the previous section we provided analytical results for the expectation values of all terms appearing in the Hamiltonian (1) with respect to the assumed wavefunction (4). These results enable us to calculate the ground state energy $W \equiv \langle \hat{H} \rangle_G$ for a fixed $|\Psi_0\rangle$. The remaining task, which we perform for a spin-isotropic and translationally invarient wavefunction, is the minimization of this energy (or of the functional $\mathcal{F} \equiv W - 2\mu_G n_G$, where $n_G \equiv \langle \hat{n}_{i\sigma} \rangle_G$), with respect to the wavefunction $|\Psi_0\rangle$. This wavefunction enters the variational problem via $n \equiv \langle \hat{n}_{i\sigma} \rangle_0$ and the lines $P_{\mathrm{l,l'}}$ and $S_{\mathrm{l,l'}}$. Since we study superconducting states, the correlated and noncorrelated numbers of particles (n_G and n) may differ, and hence it is technically easier to minimize the functional $\mathcal{F}$ at a constant chemical potential μ_G, and not the ground state energy at a constant number of particles n_G. Obviously, there is a one to one correspondence between μ_G and n_G and the latter is determined uniquely by the value of n.

The remaining variational problem leads (cf e.g. [40, 41, 63]) to the effective single-particle Schrödinger-like equation

$$\hat{H}_0^{\text{eff}} \left| \Psi_0 \right\rangle = E^{\text{eff}} \left| \Psi_0 \right\rangle, \tag{44}$$

with the self-consistently defined effective single-particle Hamiltonian

$$\hat{H}_0^{\text{eff}} = \sum_{\mathbf{i},\mathbf{j},\sigma} t_{\mathbf{i},\mathbf{j}}^{\text{eff}} \hat{c}_{\mathbf{i},\sigma}^{\dagger} \hat{c}_{\mathbf{j},\sigma} + \sum_{\mathbf{i},\mathbf{j}} \left(\Delta_{\mathbf{i},\mathbf{j}}^{\text{eff}} \hat{c}_{\mathbf{i},\uparrow}^{\dagger} \hat{c}_{\mathbf{j},\downarrow}^{\dagger} + \text{H. c.} \right), \tag{45}$$

$$t_{\mathbf{i},\mathbf{j}}^{\text{eff}} \equiv \frac{\partial \mathcal{F}\left(\left| \Psi_0 \right\rangle, x \right)}{\partial P_{\mathbf{i},\mathbf{j}}}, \quad \Delta_{\mathbf{i},\mathbf{j}}^{\text{eff}} \equiv \frac{\partial \mathcal{F}\left(\left| \Psi_0 \right\rangle, x \right)}{\partial S_{\mathbf{i},\mathbf{j}}}, \tag{46}$$

with $t_{\mathbf{i},\mathbf{j}}^{\text{eff}}$ being the effective hopping amplitude and $\Delta_{\mathbf{i},\mathbf{j}}^{\text{eff}}$ the gap function. The effective dispersion relation, the effective gap, and eigenenergies of $\hat{H}_0^{\text{eff}}$ are defined, respectively, as

$$\varepsilon^{\text{eff}}(\mathbf{k}) = \frac{1}{L} \sum_{\mathbf{i},\mathbf{j}} \exp^{i(\mathbf{i}-\mathbf{j})\mathbf{k}} t_{\mathbf{i},\mathbf{j}}^{\text{eff}} = \left[\sum_{\mathbf{j}} \exp^{i(\mathbf{i}-\mathbf{j})\mathbf{k}} t_{\mathbf{i},\mathbf{j}}^{\text{eff}} \right]_{\mathbf{i}=(0,0)}, \tag{47}$$

$$\Delta^{\text{eff}}(\mathbf{k}) = \frac{1}{L} \sum_{\mathbf{i},\mathbf{j}} \exp^{i(\mathbf{i}-\mathbf{j})\mathbf{k}} \Delta_{\mathbf{i},\mathbf{j}}^{\text{eff}} = \left[\sum_{\mathbf{j}} \exp^{i(\mathbf{i}-\mathbf{j})\mathbf{k}} \Delta_{\mathbf{i},\mathbf{j}}^{\text{eff}} \right]_{\mathbf{i}=(0,0)}, \tag{48}$$

$$E^{\text{eff}}(\mathbf{k}) = \sqrt{\varepsilon^{\text{eff}}(\mathbf{k})^2 + \Delta^{\text{eff}}(\mathbf{k})^2}, \tag{49}$$

where the last expressions for $\varepsilon^{\text{eff}}(\mathbf{k})$ and $\Delta^{\text{eff}}(\mathbf{k})$ are valid for a homogeneous system. The final solution (of one iteration of our self-consistency loop) is obtained by solving equations (44)–(46), with the additional minimization condition $\partial_x \mathcal{F}\left(\left| \Psi_0 \right\rangle, x \right) = 0$. Having solved these equations, we can make the next iteration and calculate the new $\left| \Psi_0 \right\rangle$ lines (from the definition in equation (12)), according to the prescriptions

$$P_{\mathbf{l},\mathbf{m}} = \frac{1}{L} \sum_{\mathbf{k}} e^{i\mathbf{k}(\mathbf{l}-\mathbf{m})} n_{\mathbf{k}}^0, \qquad n_{\mathbf{k}}^0 = \frac{1}{2} \left[1 - \frac{\varepsilon^{\text{eff}}(\mathbf{k})}{E^{\text{eff}}(\mathbf{k})} \right], \tag{50}$$

$$S_{\mathbf{l},\mathbf{m}} = \frac{1}{L} \sum_{\mathbf{k}} e^{i\mathbf{k}(\mathbf{l}-\mathbf{m})} \Delta_{\mathbf{k}}^0, \qquad \Delta_{\mathbf{k}}^0 = -\frac{1}{2} \frac{\Delta^{\text{eff}}(\mathbf{k})}{E^{\text{eff}}(\mathbf{k})}. \tag{51}$$

The resulting computational self-consistency loop is shown in figure 2. Note also that the self-consistency loop procedure is equivalent to the variational procedure used in [40, 41, 63], as well as in the SGA method [1, 23, 25, 26, 29, 30, 57, 64, 70, 71], as shown explicity in [80]. The convergence is achieved when the new $\left| \Psi_0 \right\rangle$ lines differ from the previous ones by less than the assumed precision value, typically 10^{-7}. Below we provide a detailed numerical analysis of the results, as well as compare them to experiment.

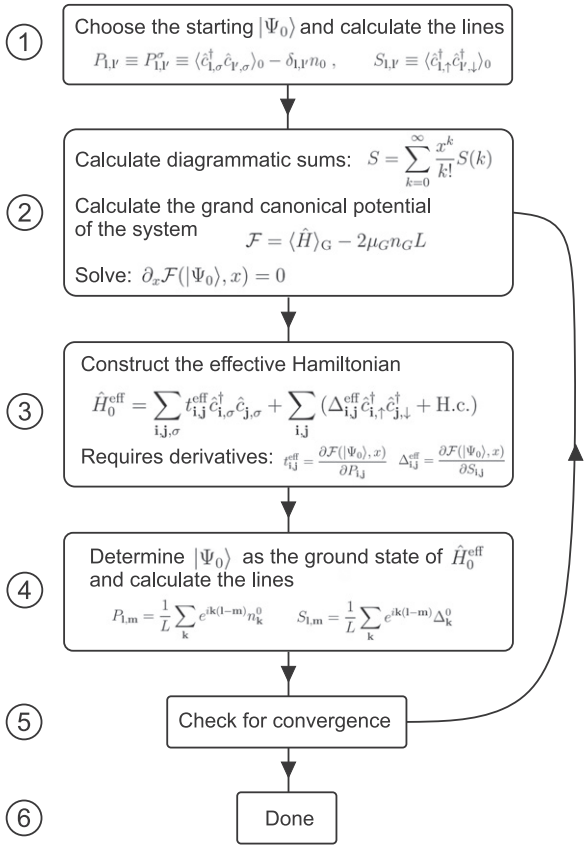

Figure 2. The full self-consistency loop of the DE-GWF method.

4. Results and their analysis

4.1. Numerical details

The self-consistency loop in figure 2 is solved numerically with the use of GNU Scientific Library (GSL). The new lines are calculated from equations (50)–(51) by numerical integration in $\mathbf{k}$ space (this corresponds to an infinite system size, $L \to \infty$). The typical accuracy of our solution procedure is equal to 10^{-7}. We set $|t| = -t$ as our unit of energy, and present the results for $t' = 0.25$ and $J = 0.3$, unless stated otherwise. We consider the two cases with $c = 0$ and $c = 1$, but, as their results are very close, we show the $c = 0$ data only in figures 4 and 5(a). In several figures we also provide the results of the GCGA (and GA) methods, which were obtained by the simplified zeroth-order DE-GWF method (equivalent to GCGA or GA, as discussed in section 2.5).

For most cases, we carry out the expansion to the fifth order, which provides quite accurate results. The lower-order results are also exhibited in selected figures to visualize our method's convergence. To calculate the diagrammatic sums we need to neglect long-range $|\Psi_0\rangle$ lines in real space. Namely, we take as nonzero only the lines $P_{\mathbf{i},\mathbf{j}} \equiv P_{0,(\mathbf{i}-\mathbf{j})} \equiv P_{XY}$ (with $X = i_1 - j_1$, $Y = i_2 - j_2$), for which $X^2 + Y^2 \leqslant R^2 = 25$ (i.e. with up to 14th neighbors). The same condition applies for $S_{\mathbf{i},\mathbf{j}}$, $t^{\mathrm{eff}}_{\mathbf{i},\mathbf{j}}$, and $\Delta^{\mathrm{eff}}_{\mathbf{i},\mathbf{j}}$. We also define an additional convergence parameter. Namely, we

take into account only those contributions to the diagrammatic sums in which the total Manhattan distance (i.e. $|X| + |Y|$) of all lines is smaller than R_{tot}, typically set to $R_{\text{tot}} = 26$.

In total, we have the three convergence parameters: (i) order k, (ii) $|\Psi_0\rangle$ cutoff radius R, and (iii) total Manhattan distance of all lines R_{tot}. The uncertainty of our results coming from parameters (ii) and (iii) is of the order of the line thickness of the presented curves, whereas the kth-order results for most doping values are between the $k-1$ and $k-2$ order results (and the differences between them diminish with the increasing k). Therefore, we believe that the series is convergent. The accuracy of our results may be further improved by including higher-order terms. However, the number of diagrams grows exponentially with the increasing order, which makes the analysis for higher orders computationally demanding.

4.2. Comparison with variational Monte Carlo results

To test our approach, in figures 3(a) and (b) we have compared our results with those of [9] obtained by the variational Monte Carlo (VMC) method for the Hamiltonian with $c = 1$ and for the values of parameters $t' = J = 0.3$. In order to obtain comparable results we have to truncate our effective Hamiltonian, as in VMC, so that it contains parameters only up to next-nearest neighbors (see appendix E for details). We call the resulting approach VMC-like DE-GWF. Its results agree very well with those of VMC. The sources of small quantitative discrepancies between the two results are approximations of both methods. First, in VMC calculations, a finite-size 11×11 (or 13×13) lattice is used, whereas we use an infinite lattice in the DE-GWF method. Note that in an analogous comparison [28] with VMC calculations performed for the Hubbard model on an 8×8 lattice, the discrepancies were much larger. The finite-size error of VMC can be estimated by noting that the 11×11- and 13×13-lattice VMC results in figures 3(a) and (b) do not follow a continuous curve, but are scattered around the VMC-like DE-GWF curve. Second, in our method we perform the expansion up to the terms with diagrams containing $l = 15$ lines (the remaining error coming from the $|\Psi_0\rangle$ cutoff in real space is of the order of the line thickness). Note that the $l = 15$, 13, and 11 results are very close to each other.

Additionally, discrepancies might come from the fact that in our procedure the correlated (n_G) and uncorrelated (n) numbers of particles are slightly different, whereas it is not clear to us from [9] if there is a change in the particle number there due to the Gutzwiller projection.

The difference between the VMC-like DE-GWF and the full DE-GWF scheme shows that neglecting longer-range gap and hopping components can lead to a decrease of the principal gap component by up to 37% (the largest discrepancy is near half filling) and the corresponding decrease of the condensation energy by $3 \div 35\%$ (the largest discrepancy is for the overdoped system). These discrepancies are larger than those observed in [43], in which the longer-range *hopping* components were not included. Our results suggest that inclusion of the longer-range effective parameters is important, as it can lead to changes of results even by a factor of ≈ 1.6, even though the condensation energy does not change much. We also provide GA and GCGA results to show their qualitative differences with respect to both VMC and DE-GWF. Surprisingly, the GA is closer to the VMC and the DE-GWF results than its extended variant, the GCGA. The largest discrepancy between GA and either VMC or DE-GWF data is for underdoped ($\delta < 0.15$) and overdoped $\delta > 0.3$ systems. We have also verified that for the zeroth order the VMC-like and the full DE-GWF methods yield the same results, as they

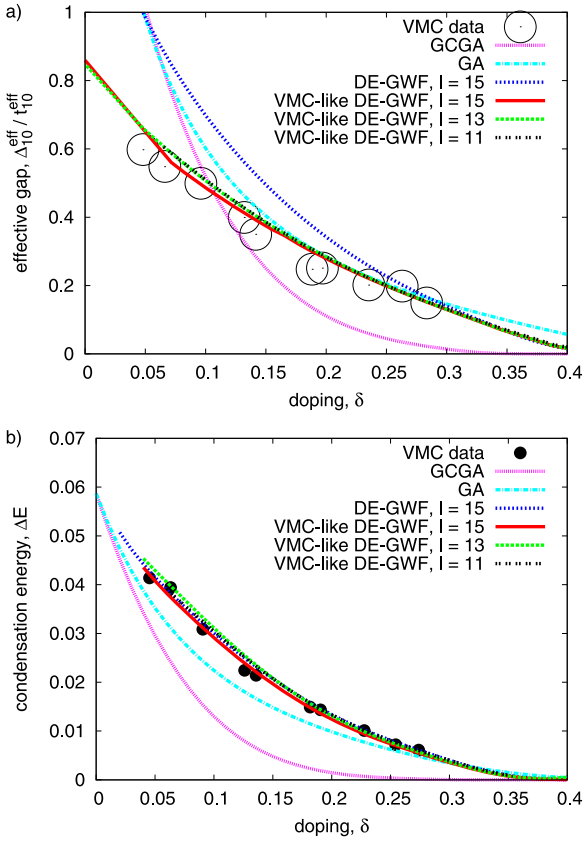

Figure 3. Comparison of DE-GWF (lines) for $J = 0.3$ and $t' = 0.3$ with variational Monte Carlo (VMC) results (the point size is equal to the error; from [9]). (a) Effective gap (in units of $t_{10}^{\rm eff}$) and (b) condensation energy as a function of doping. The VMC-like DE-GWF lines are obtained with an effective single-particle Hamiltonian containing only (next-) nearest-neighbor and on-site terms (see appendix E for details). For the (VMC-like) DE-GWF results labelled with $l = 15$, 13, and 11 we include diagrams with up to l lines when computing the diagrammatic sums. The GA and GCGA results are obtained by the truncated zeroth-order DE-GWF.

should, because the zeroth-order diagrammatic sums only contain lines connecting (next) nearest neighbors.

4.3. Comparison to experiment and discussion

The break in the VMC-like DE-GWF curve in figure 3(a) appearing at $\delta \approx 4\%$ is related to the phase separation effect present for the SC phase in the t–J model in both (VMC-like) DE-GWF and VMC methods [6, 24, 50]. Namely, the chemical potential (μ_G) of the SC phase has a maximum as a function of doping for $\delta \approx 3$–5%. For this reason, our numerical procedure (in which μ_G is increased at each step) fails to converge for $\delta \lesssim 5\%$. To obtain the following DE-GWF results we changed our method to work with a fixed n_G (similarly as in [1, 23, 29], with an additional equation for n_G). This allowed us to obtain convergence in the vicinity of the half filling.

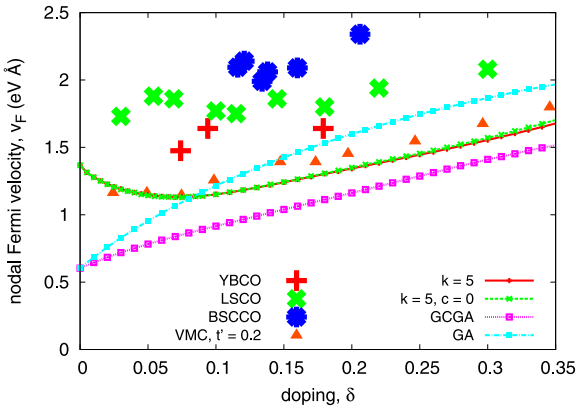

Figure 4. Universal Fermi velocity in the nodal ($k_x = k_y$) direction as a function of doping. The experimental values are taken from [8] and references therein, and typically have an uncertainty of 20%. The VMC results are taken from [69]. The results obtained for the model with and without the density–density term (for $c = 0$ and $c = 1$, respectively) are very close.

One of the most important physical characteristics of the cuprates is the universal nodal Fermi velocity v_F (i.e., v_F is independent of δ) [75]. Recently however, it has been shown that the Fermi velocity for the underdoped samples exhibits a low-energy kink and a nontrivial doping dependence [62]. In effect, the velocity possesses two components: one near the Fermi surface, which is doping dependent, and the velocity slightly below the Fermi surface, which is doping independent. The source of the kink in the dispersion is probably the electron–phonon interaction [27] and is not included in our purely electronic model. In figure 4 we show the Fermi velocity defined as $v_F = \nabla_{\mathbf{k}} \epsilon^{\mathrm{eff}}(\mathbf{k})\big|_{\epsilon^{\mathrm{eff}}(\mathbf{k})=0}$. Its behavior agrees with the experimental results (we assume the lattice constant $a = 4$ Å and $|t| = 0.35$ eV). The RMFT method does not reproduce such behavior [8, 26]. We also present for comparison the VMC results [48, 49, 51, 68] obtained in [69] for $t' = 0.2$. The weak doping dependence of the Fermi velocity speaks in favor of a transfer of the spectral density to the nodal direction from the antinodal direction with the decreasing doping (see also the discussion below).

In figure 5 we plot the two gaps: the effective gap at the antinodal point $\Delta^{\mathrm{eff}}_{\mathbf{k}=(\pi,0)}$ and the correlated gap $\Delta_G \equiv \left\langle \hat{c}^{\dagger}_{\mathbf{i}\uparrow} \hat{c}^{\dagger}_{\mathbf{j}\downarrow} \right\rangle_G$. The effective gap agrees with the experimental values only after rescaling by a factor of 0.4 (not shown), similarly as for the GA [8] and VMC [49] approaches. Recent experiments have shown, however, that the competition between the superconducting gap and pseudogap [11, 52, 54] in BSCCO diminishes essentially the value of the superconducting gap in the nodal direction [31–33]. In fact, this gap is shown to vanish for underdoped samples [33]. Therefore, a quantitative agreement with the experimental points in figure 5(a) should not be the goal in describing high-temperature superconductors, as including the pseudogap may change the picture essentially. One should also keep in mind that $\Delta^{\mathrm{eff}}_{\mathbf{k}=(\pi,0)}$ depends on J. For lower J values we obtain much better agreement with the experiment (but at the same time, the agreement of the nodal Fermi velocity is then worse). Similarly to the case in VMC calculations [66], we observe an exponential decay of the gap with the doping reaching

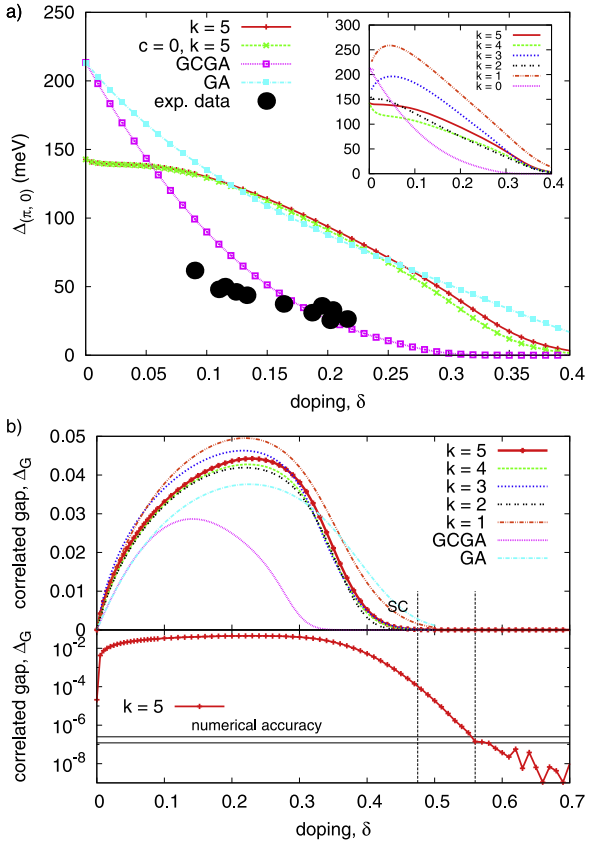

Figure 5. (a) The effective gap at the antinodal point $\Delta^{\mathrm{eff}}_{\mathbf{k}=(\pi,0)}$ and its comparison with the experimental data of [55]; (b) the correlated gap $\Delta_G \equiv \left\langle \hat{c}^{\dagger}_{\mathbf{i}\uparrow}\hat{c}^{\dagger}_{\mathbf{j}\downarrow}\right\rangle_G$. In (a) the gap values are plotted in physical units (assuming $t = 0.35$ eV). The zeroth- to fifth-order results are exhibited to demonstrate the method convergence, cf inset. In (b) we show also the gap on the logarithmic scale in the lower panel. We mark our numerical accuracy limit, which is around 10^{-7}, by the two horizontal lines. A residual very small gap persists to the dopings beyond the upper critical concentration (see also main text).

the upper critical concentration $\delta_c \sim 1/2$. We term as SC the phase with $\Delta_G > 10^{-4}$, which corresponds to gap values of the order of 0.4 K, below which other effects can destabilize the superconductivity. In our model situation, however, we still have a stable superconducting solution even if we increase doping above such defined δ_c by 8%, as shown in figure 5(b) (bottom panel) . One must note that if the experimentally measured gap is usually determined for temperature $T \gtrsim 1$K then the tail of $\Delta_G(\delta)$ beyond δ_c will not be detected, as then effectively $T > T_c$. Also, we have neglected here the atomic disorder. In the inset to figure 5(a) and in the upper panel to figure 5(b) we show also the order-of-expansion dependence of the results. It can be seen that, for most of the doping values, the kth-order results are between the results obtained for orders $k-1$ and $k-2$. Moreover, the difference between the orders diminishes with increasing order.

An important qualitative feature of the results displayed in figures 3(a), 4, and 5(a) and (b) should be noted. Namely, the SGA method provides a good semiquantitative behavior of the

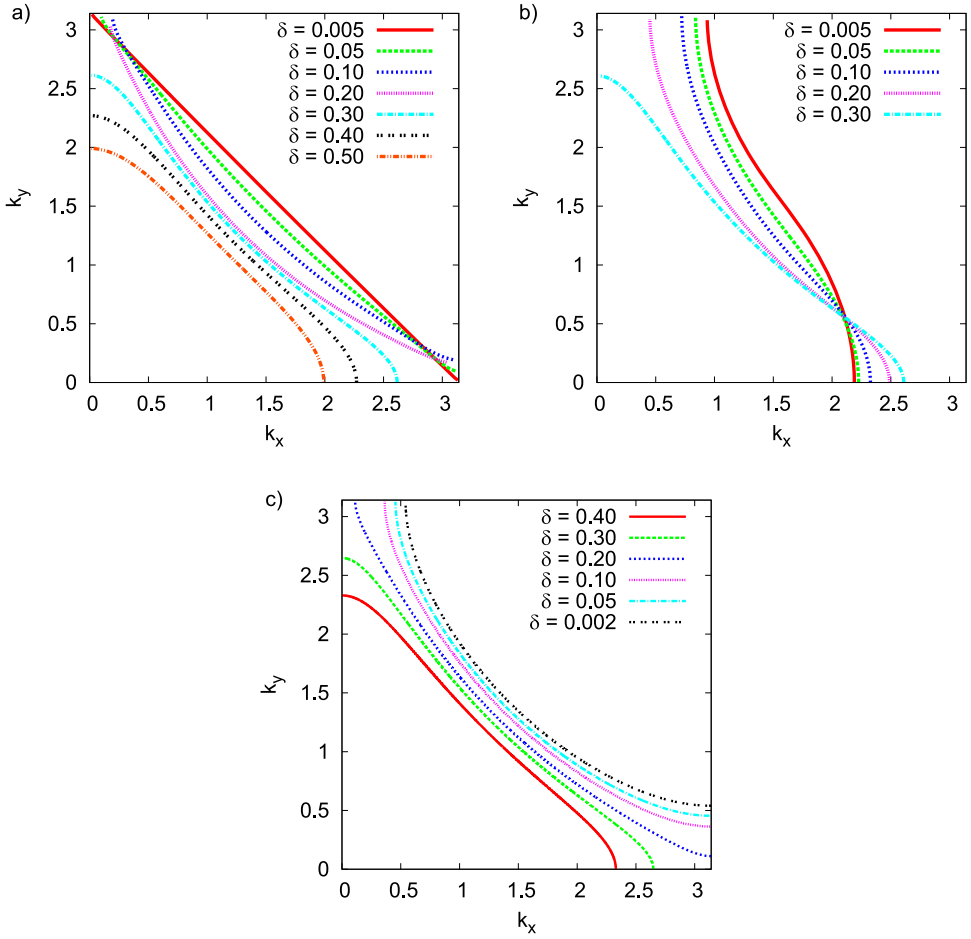

Figure 6. (a) Fermi surfaces for selected values of doping in the normal phase (a), the spontaneously distorted Pomeranchuk phase (b), and the bare Hamiltonian with only kinetic energy without renormalization (c).

data in figures 5(a) and (b). However, it fails in the case of the data shown in figures 3(a) and 4, whereas the DE-GWF method provides a good overall representation of all the data analyzed. Also, the agreement with the VMC results in figure 3(b) is excellent. Hence the DE-GWF method seems to us to be the method providing a coherent set of results for the ground state of an infinite-lattice system. Obviously, the approach still requires generalization of the analysis to nonzero temperature and applied magnetic field.

In figure 6 we exhibit the doping dependence of the Fermi-surface topology, starting from the effective Hamiltonian (45). We also show results for the state with a spontaneously broken rotational symmetry, i.e. the appearance of the so-called Pomeranchuk phase [20, 25, 65]. This phase has also been investigated by VMC [9, 74]. It is characterized by the symmetry breakdown, i.e. $t_x^{\mathrm{eff}} \neq t_y^{\mathrm{eff}}$, where x and y are the directions in the (x, y) plane. The drawback of using VMC in such calculations is that the finite-size effects become much more important than for the description of the SC phase (typically 12×12 points [74] or 8×8 points [9] are included within one-quarter of the Brillouin zone, cf also the discussion in [9]). Our method does not suffer from those finite-size limitations, and therefore it seems more appropriate for analyzing

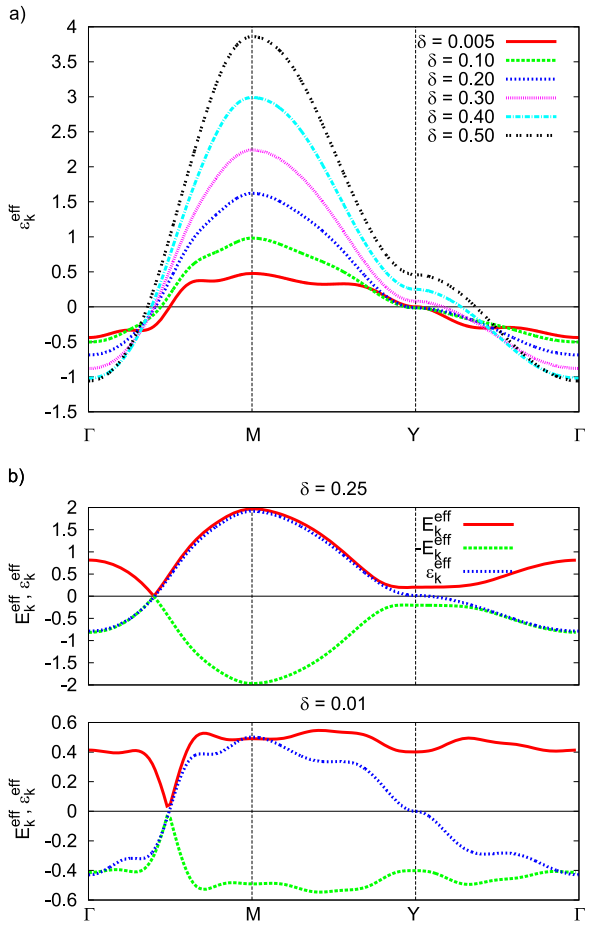

Figure 7. (a) Dispersion relation of the effective Hamiltonian for the normal (paramagnetic) phase. The vertical lines mark specific points of the Brillouin zone: $\Gamma = (0, 0)$, $\mathrm{M} = (\pi, \pi)$, and $\mathrm{Y} = (0, \pi)$. The horizontal line at $\varepsilon_{\mathbf{k}}^{\mathrm{eff}} = 0$ marks the Fermi energy. (b) SC-phase quasiparticle energies for two doping values; the energies $\varepsilon_{\mathbf{k}}^{\mathrm{eff}}$ (of the normal phase at the same doping) are drawn for comparison.

the Fermi-surface properties. It can be seen from figure 6(b) that the correlated Fermi surface differs essentially from that for noninteracting particles near half filling. Namely, if we approach the half-filled case the Fermi surface becomes a line as in a bare Hamiltonian with the n.n. hopping only. This is caused by diminishing of certain effective hopping parameters in the vicinity of half filling (as shown explicitly in figure 8 (b)). The doping dependence of the Fermi surface in the Pomeranchuk phase is similar to that obtained in the Hubbard model [5]. The role of the Pomeranchuk instability will not be studied in detail here.

The dispersion relation in the normal phase and the quasiparticle energies in the superconducting state are shown in figures 7(a) and (b), respectively. With decreasing doping, the bandwidth becomes smaller, and the dispersion deviates significantly from the simple form with the dominating n.n. hopping. The SC-phase quasiparticle energies (shown in figure 7(b)) resemble the metallic dispersion $\varepsilon_{\mathbf{k}}^{\mathrm{eff}}$ only for substantial doping values. With decreasing doping the deviations from the effective gap become larger. This effective gap has its maximum value

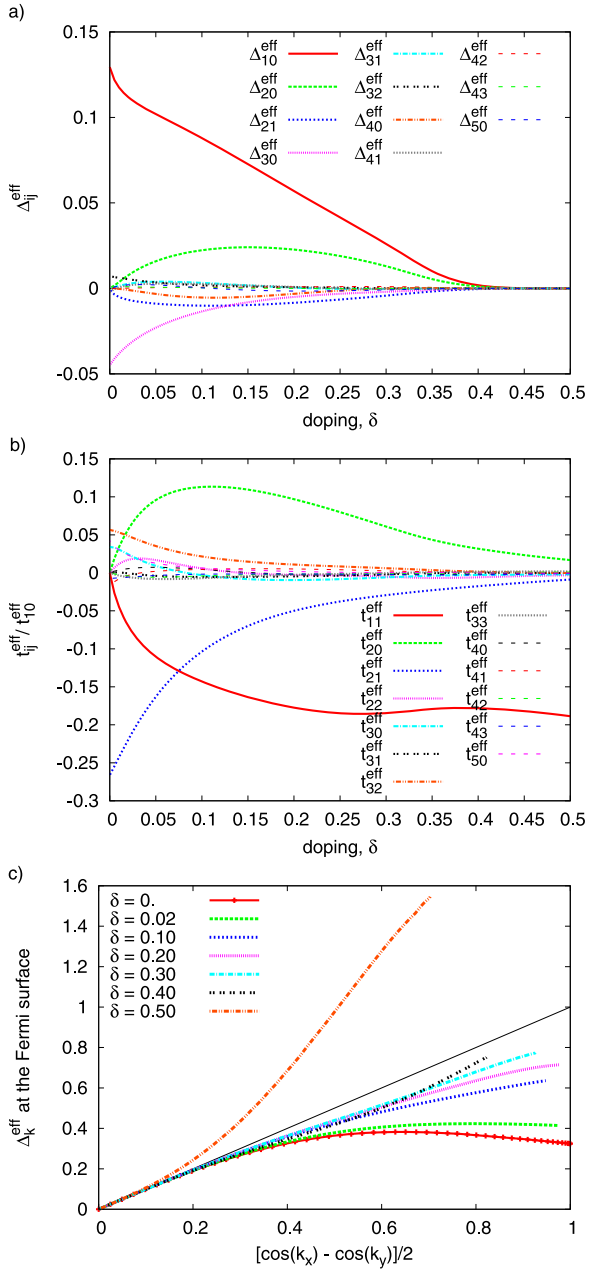

Figure 8. (a) Effective gap parameters obtained variationally as a function of doping; (b) effective hopping parameters relative to the dominant t_{10}^{eff} contribution; (c) effective gap in momentum space at the Fermi energy for selected doping values. The black line corresponds to a pure $d_{x^2-y^2}$ dependence. The gaps are normalized for clarity.

(in the antinodal direction) close to the Y point of the Brillouin zone. For small doping values this gap is comparable to the maximum value of $\varepsilon_{\mathbf{k}}^{\mathrm{eff}}$.

In the panel composing figure 8 we detail the effective gap and the effective hopping amplitudes. Near half filling, only a few components of the gap are of substantial magnitude, namely $\Delta_{10}^{\mathrm{eff}}$, $\Delta_{21}^{\mathrm{eff}}$ (small, but nonzero), $\Delta_{30}^{\mathrm{eff}}$, and $\Delta_{32}^{\mathrm{eff}}$, as also found in [43] (in which [31] and

[40] are the most distant gap components). The same components of the effective *hopping* are nonzero at half filling, together with additional ones (e.g. t_{50}^{eff}). From figure 8(c) it follows that the effective gap along the Fermi surface deviates from a pure $d_{x^2-y^2}$ form, especially close to half-filling, for which the gap in the antinodal direction is diminished by a factor of 3 with respect to the pure $d_{x^2-y^2}$ form. Such deviations are also observed in high-temperature superconductors [31–33, 38, 42, 60, 61, 68], where the situation is complicated further by the appearance of a pseudogap [11, 13, 54]. Namely, for the underdoped samples the *total* gap measured in angle-resolved photoemission spectroscopy (ARPES) is increased in the antinodal direction with respect to the pure $d_{x^2-y^2}$ component [38, 42, 60, 61, 68], but the spectral weight corresponding to the *superconducting gap* is simultaneously decreased [31–33], which agrees with our findings in figure 8(c). Therefore, the decrease of superconducting gap can be an intrinsic effect for strongly correlated superconductors, not only caused by the competition with the pseudogap.

5. Summary and outlook

5.1. Method comparison

When working with a variational Gutzwiller wavefunction, the main task is the calculation of the expectation value (equation (9)) of the Hamiltonian with respect to this trial wavefunction. So far, there have been two types of method to approach this problem. In one of them (GA and the derivatives) the expectation values of the Hamiltonian terms are approximated by the corresponding expectation values with respect to the noncorrelated wavefunction ($|\Psi_0\rangle$) multiplied by appropriate renormalization factors (e.g. $\left\langle \hat{c}^{\dagger}_{\mathbf{i},\sigma}\hat{c}_{\mathbf{j},\sigma}\right\rangle_G^{(GA)} = g_t \left\langle \hat{c}^{\dagger}_{\mathbf{i},\sigma}\hat{c}_{\mathbf{j},\sigma}\right\rangle_0$). This yields a very fast method, but constitutes an additional approximation, which prevents the description of superconductivity or Pomeranchuk phase in the Hubbard model. From figure 3 it can be seen that such a method is able to yield quite accurate results for the condensation energy and the effective gap in the *t*–*J* model. However, as we show in appendix C, this does not mean that the GA is able to reproduce all the VMC (or DE-GWF) results accurately. For example, the average values of hopping terms are underestimated within the GA by a factor of two already at the doping $\delta \approx 17\%$. The extended GCGA method compares much worse against the VMC (or DE-GWF) results than the original GA. It is difficult to judge for what reasons one approximate scheme is better than the other, and therefore we cannot identify why the GCGA is less accurate than the GA in the studied situation.

In contrast, the VMC approach evaluates the expectation values in a controlled manner, but on a relatively small lattice, which leads to an increased numerical complexity of the approach with growing system size. In the DE-GWF method the averages are also calculated as accurately as possible, but a different path towards computing them is undertaken. The resultant procedure leads to principal advantages over the VMC approach: (i) the absence of the finite-size limitations, (ii) relatively low computational complexity, (iii) the ability to account for longer-range effective parameters in a natural manner, and (iv) the possibility of extending the approach to nonzero temperatures. On the other hand, the VMC approach can be easily extended by introducing additional Jastrow factors to the trial wavefunction (this yields wavefunctions with, e.g., the doublon–holon correlation [66, 67] or Baeriswyl wavefunctions

[4, 12, 22]). Investigation of the possibility of extending the DE-GWF method in this direction is planned.

5.2. Comparison with the Hubbard model results and the experimental data

As the paper contains a new method of approach (DE-GWF) to high-temperature superconductivity analyzed within the t–J model, a methodological note is in order here. Namely, we would like to relate the present results to those from our very recent analysis of the Hubbard model within the DE-GWF approach [28]. First, the 'dome-like' shape of $\Delta_G(\delta)$ is similar in both situations, particularly in the large-U limit for the Hubbard model, though the upper critical concentration is lower in the latter case. Second, the doping independence of the Fermi velocity $v_F(\delta)$, representing a crucial test for any theory, is also closer to the experimental values in the Hubbard-model case. In both situations, the DE-GWF approach provides much better values than those obtained within the dynamic mean-field theory (DMFT) [7]. Third, the doping dependence of the gap in the antinodal direction (cf figure 5(a)) can reproduce the experimental trend if we rescale the results by a factor of $\sim 1/2$ (see also below). Fourth, the deviations of the gap value along the Fermi surface from the $d_{x^2-y^2}$-wave symmetry are consistent with the experimental trend: the diminishing of the superconducting gap in the antinodal region for underdoped samples.

5.3. Outlook and critical remarks

Combining the above features, together with the good agreement of the present results with the VMC analysis for small systems, the DE-GWF approach provides a unique method of accounting for the basic superconducting properties in a quantitative manner. However, it fails to address one principal property, namely the appearance of the pseudogap. Very recently, we have generalized the analysis of the projected t–J model [59] by introducing in a systematic manner its supersymmetric (spin-fermion) representation. In this new representation the Fermi sector provides essentially the t–J model in the above fermionic representation, with an additional renormalization of both the hopping and the kinetic exchange integral amplitudes. This should diminish the scale of energies obtained theoretically in figure 5(a) (this idea still requires a detailed numerical analysis). What is even more interesting, the newest model [59] provides an explicit pairing and a separate scale of excitations in the Bose sector, which may be interpreted as an appearance of a pseudogap. Summarizing, the new model preserves essential features of the t–J model as discussed here, but introduces additionally the bosonic branch of collective phenomena. Such division is implicit in the recent calculations [13]. Work along this line is in progress and, as it requires a very complex numerical analysis, will be presented separately in the near future.

In conclusion, it is in our view rewarding that the Hubbard and the t–J models provide converging results within the DE-GWF approach, at least on a semiquantitative level. The application of the method thus corrects some of the SGA results [25, 26] and goes beyond the standard RMFT [10, 15, 16, 26, 34, 46, 63, 72] approach.

To what extent this analysis can be enriched on the same level by a multiband model [21], remains to be seen.

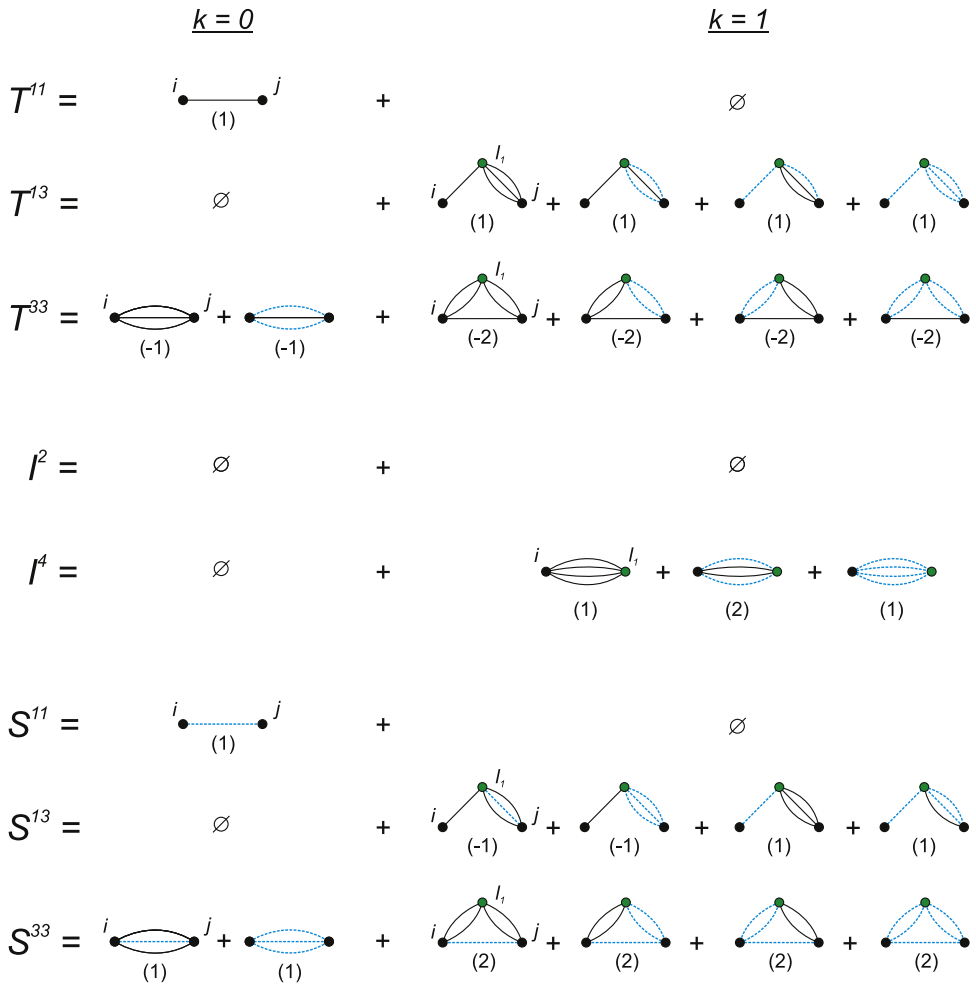

Figure A1. Diagrams in the zeroth and the first order. The superconducting (paramagnetic) contractions $S_{l,l'}$ ($P_{l,l'}$) are marked with dashed (solid) lines. The internal (external) vertices are marked with green (black) circles. The numbers in brackets below diagrams represent their multiplicity (a combinatorial factor).

Acknowledgments

The work was supported in part by the Foundation for Polish Science (FNP) under the 'TEAM' program, as well as by the project 'MAESTRO' from the National Science Centre (NCN), No DEC-2012/04/A/ST3/003420. Part of the computational work was performed on the Shiva supercomputer (IF UJ). One of the authors (JK) acknowledges the hospitality of the Leibniz Universität in Hannover during the finalization of the paper, whereas JB thanks the Jagiellonian University for its hospitality during the early stage of the work.

Note added in proof. Renormalization of the effective hopping component t_{11}^{eff} to zero upon approaching half-filling (cf figure 8(b)), was pointed out previously in [76].

Appendix A. Exemplary types of diagrams

In figure A1 we present the diagram types for the kinetic energy (T^{11}, T^{13}, T^{33}), the potential energy (I^2, I^4), and the 'correlated delta' (S^{11}, S^{13}, S^{33}) diagrammatic sums. We consider the first two orders (i.e. the diagrams with zero and one internal vertex). For the paramagnetic phase we would have only the diagrams without dashed lines (and obviously, no correlated delta diagrams). The number of diagrams grows exponentially with increasing order k, and therefore we determine these diagrams by means of a numerical procedure.

The general form of the resulting diagrammatic sums is obtained as e.g.

$$T^{11} = P_{ij} + O\left(x^2\right), \tag{A.1}$$

$$T^{13} = x\sum_{l_1}\left(P_{il_1}P_{jl_1}^3 + P_{il_1}P_{jl_1}S_{jl_1}^2 + S_{il_1}P_{jl_1}^2S_{jl_1} + S_{il_1}S_{jl_1}^3\right) + O\left(x^2\right), \tag{A.2}$$

$$S^{13} = x\sum_{l_1}\left(-P_{il_1}P_{jl_1}^2S_{jl_1} - P_{il_1}S_{jl_1}^3 + S_{il_1}P_{jl_1}^3 + S_{il_1}S_{jl_1}^2P_{jl_1}\right) + O\left(x^2\right). \tag{A.3}$$

In order to perform the summations of diagrams over a lattice, we need to assume as nonzero the $\left|\Psi_0\right\rangle$ lines up to some finite distance. In the main text we have taken as nonzero the lines ($S_{\mathbf{i},\mathbf{j}} \equiv S_{X,Y}$ with $X = \left(i_1 - j_1\right)$, $Y = \left(i_2 - j_2\right)$, $P_{X,Y}$–analogously) fulfilling $X^2 + Y^2 \leqslant R^2 = 25$. If the cutoff distance is defined by $X^2 + Y^2 \leqslant 2$, then they are as follows:

$$T^{11}(0) = P_{10}, \tag{A.4}$$

$$T^{33}(0) = -P_{10}^3 - P_{10}S_{10}^2, \tag{A.5}$$

$$T^{13}(1) = 2P_{10}^3P_{11} + 2P_{10}P_{11}^3 + 2P_{10}P_{11}S_{10}^2. \tag{A.6}$$

Increasing the cutoff distance R leads to significant complication of the obtained expressions—e.g., for $X^2 + Y^2 \leqslant 4$ (allowing for nonzero P_{20} and S_{20} lines), we have

$$\begin{aligned} T^{13}(1) = {} & 2P_{10}^3P_{11} + 2P_{10}P_{11}^3 + 2P_{10}P_{11}S_{10}^2 + P_{10}^3P_{20} + S_{10}S_{20}^3 + P_{10}^2S_{10}S_{20} \\ & + P_{20}^2S_{10}S_{20} + 2P_{10}P_{11}S_{10}^2 + S_{10}^3S_{20} + P_{10}P_{20}S_{20}^2. \end{aligned} \tag{A.7}$$

In our numerical procedure, when calculating the diagrammatic sums, we start from the general form (as in equations (A.1)–(A.3)) and sum over the internal vertex positions (here over $\mathbf{l}_1$), making sure that the condition $X^2 + Y^2 \leqslant 25$ is fulfilled for all contributing lines $P_{X,Y}$, $S_{X,Y}$.

Appendix B. Exchange term evaluation

The expressions for the components of the exchange term are as follows (with $m_{\mathbf{i}} \equiv n_{\mathbf{i}\uparrow} - n_{\mathbf{i}\downarrow}$):

$$\frac{1}{4}\left\langle \hat{n}_{\mathrm{i}}\hat{n}_{\mathrm{j}}\right\rangle_{G} = +\frac{n_{\mathrm{i}}n_{\mathrm{j}}}{4} + \frac{\left(n_{\mathrm{i}}-1\right)\left(n_{\mathrm{j}}-1\right)I^{42}_{\mathrm{ij}\downarrow}}{2\left(n_{\mathrm{i}\downarrow}-1\right)\left(n_{\mathrm{i}\uparrow}-1\right)\left(n_{\mathrm{j}\downarrow}-1\right)} + \frac{\left(n_{\mathrm{i}}-1\right)\left(n_{\mathrm{j}}-1\right)I^{42}_{\mathrm{ij}\uparrow}}{2\left(n_{\mathrm{i}\downarrow}-1\right)\left(n_{\mathrm{i}\uparrow}-1\right)\left(n_{\mathrm{j}\uparrow}-1\right)}$$
$$+ \frac{\left(n_{\mathrm{i}}-1\right)\left(n_{\mathrm{j}}-1\right)I^{24}_{\mathrm{i}\downarrow\mathrm{j}}}{2\left(n_{\mathrm{i}\downarrow}-1\right)\left(n_{\mathrm{j}\downarrow}-1\right)\left(n_{\mathrm{j}\uparrow}-1\right)} + \frac{\left(n_{\mathrm{i}}-1\right)\left(n_{\mathrm{j}}-1\right)I^{22}_{\mathrm{i}\downarrow\mathrm{j}\downarrow}}{4\left(n_{\mathrm{i}\downarrow}-1\right)\left(n_{\mathrm{j}\downarrow}-1\right)}$$
$$+ \frac{\left(n_{\mathrm{i}}-1\right)\left(n_{\mathrm{j}}-1\right)I^{22}_{\mathrm{i}\downarrow\mathrm{j}\uparrow}}{4\left(n_{\mathrm{i}\downarrow}-1\right)\left(n_{\mathrm{j}\uparrow}-1\right)} + \frac{\left(n_{\mathrm{i}}-1\right)\left(n_{\mathrm{j}}-1\right)I^{24}_{\mathrm{i}\uparrow\mathrm{j}}}{2\left(n_{\mathrm{i}\uparrow}-1\right)\left(n_{\mathrm{j}\downarrow}-1\right)\left(n_{\mathrm{j}\uparrow}-1\right)}$$
$$+ \frac{\left(n_{\mathrm{i}}-1\right)\left(n_{\mathrm{j}}-1\right)I^{22}_{\mathrm{i}\uparrow\mathrm{j}\downarrow}}{4\left(n_{\mathrm{i}\uparrow}-1\right)\left(n_{\mathrm{j}\downarrow}-1\right)} + \frac{\left(n_{\mathrm{i}}-1\right)\left(n_{\mathrm{j}}-1\right)I^{22}_{\mathrm{i}\uparrow\mathrm{j}\uparrow}}{4\left(n_{\mathrm{i}\uparrow}-1\right)\left(n_{\mathrm{j}\uparrow}-1\right)}$$
$$+ \frac{I^{2}_{\mathrm{j}\uparrow}n_{\mathrm{i}}\left(n_{\mathrm{j}}-1\right)}{4\left(n_{\mathrm{j}\uparrow}-1\right)} + \frac{I^{2}_{\mathrm{j}\downarrow}n_{\mathrm{i}}\left(n_{\mathrm{j}}-1\right)}{4\left(n_{\mathrm{j}\downarrow}-1\right)} + \frac{I^{2}_{\mathrm{i}\uparrow}\left(n_{\mathrm{i}}-1\right)n_{\mathrm{j}}}{4\left(n_{\mathrm{i}\uparrow}-1\right)} + \frac{I^{4}_{\mathrm{i}}\left(n_{\mathrm{i}}-1\right)n_{\mathrm{j}}}{2\left(n_{\mathrm{i}\downarrow}-1\right)\left(n_{\mathrm{i}\uparrow}-1\right)}$$
$$+ \frac{I^{44}_{\mathrm{ij}}\left(n_{\mathrm{i}}-1\right)\left(n_{\mathrm{j}}-1\right)}{\left(n_{\mathrm{i}\downarrow}-1\right)\left(n_{\mathrm{i}\uparrow}-1\right)\left(n_{\mathrm{j}\downarrow}-1\right)\left(n_{\mathrm{j}\uparrow}-1\right)} + \frac{I^{2}_{\mathrm{i}\downarrow}\left(n_{\mathrm{i}}-1\right)n_{\mathrm{j}}}{4\left(n_{\mathrm{i}\downarrow}-1\right)}$$
$$+ \frac{I^{4}_{\mathrm{j}}n_{\mathrm{i}}\left(n_{\mathrm{j}}-1\right)}{2\left(n_{\mathrm{j}\downarrow}-1\right)\left(n_{\mathrm{j}\uparrow}-1\right)}. \tag{B.1}$$

$$\left\langle \hat{S}^{z}_{\mathrm{i}}\hat{S}^{z}_{\mathrm{j}}\right\rangle_{G} = \frac{m_{\mathrm{i}}m_{\mathrm{j}}}{4} + \frac{m_{\mathrm{i}}\left(m_{\mathrm{j}}+1\right)I^{42}_{\mathrm{ij}\downarrow}}{2\left(n_{\mathrm{i}\downarrow}-1\right)\left(n_{\mathrm{i}\uparrow}-1\right)\left(n_{\mathrm{j}\downarrow}-1\right)} - \frac{m_{\mathrm{i}}\left(1-m_{\mathrm{j}}\right)I^{42}_{\mathrm{ij}\uparrow}}{2\left(n_{\mathrm{i}\downarrow}-1\right)\left(n_{\mathrm{i}\uparrow}-1\right)\left(n_{\mathrm{j}\uparrow}-1\right)}$$
$$- \frac{\left(-m_{\mathrm{i}}-1\right)m_{\mathrm{j}}I^{24}_{\mathrm{i}\downarrow\mathrm{j}}}{2\left(n_{\mathrm{i}\downarrow}-1\right)\left(n_{\mathrm{j}\downarrow}-1\right)\left(n_{\mathrm{j}\uparrow}-1\right)} + \frac{\left(-m_{\mathrm{i}}-1\right)\left(-m_{\mathrm{j}}-1\right)I^{22}_{\mathrm{i}\downarrow\mathrm{j}\downarrow}}{4\left(n_{\mathrm{i}\downarrow}-1\right)\left(n_{\mathrm{j}\downarrow}-1\right)}$$
$$+ \frac{\left(-m_{\mathrm{i}}-1\right)\left(1-m_{\mathrm{j}}\right)I^{22}_{\mathrm{i}\downarrow\mathrm{j}\uparrow}}{4\left(n_{\mathrm{i}\downarrow}-1\right)\left(n_{\mathrm{j}\uparrow}-1\right)} - \frac{\left(-m_{\mathrm{i}}+1\right)m_{\mathrm{j}}I^{24}_{\mathrm{i}\uparrow\mathrm{j}}}{2\left(n_{\mathrm{i}\uparrow}-1\right)\left(n_{\mathrm{j}\downarrow}-1\right)\left(n_{\mathrm{j}\uparrow}-1\right)}$$
$$+ \frac{\left(-m_{\mathrm{i}}+1\right)\left(-m_{\mathrm{j}}-1\right)I^{22}_{\mathrm{i}\uparrow\mathrm{j}\downarrow}}{4\left(n_{\mathrm{i}\uparrow}-1\right)\left(n_{\mathrm{j}\downarrow}-1\right)} + \frac{\left(-m_{\mathrm{i}}+1\right)\left(1-m_{\mathrm{j}}\right)I^{22}_{\mathrm{i}\uparrow\mathrm{j}\uparrow}}{4\left(n_{\mathrm{i}\uparrow}-1\right)\left(n_{\mathrm{j}\uparrow}-1\right)}$$
$$+ \frac{I^{2}_{\mathrm{j}\uparrow}m_{\mathrm{i}}\left(1-m_{\mathrm{j}}\right)}{4\left(1-n_{\mathrm{j}\uparrow}\right)} + \frac{I^{2}_{\mathrm{j}\downarrow}m_{\mathrm{i}}\left(-m_{\mathrm{j}}-1\right)}{4\left(1-n_{\mathrm{j}\downarrow}\right)} - \frac{I^{2}_{\mathrm{i}\uparrow}\left(-m_{\mathrm{i}}+1\right)m_{\mathrm{j}}}{4\left(n_{\mathrm{i}\uparrow}-1\right)}$$
$$+ \frac{I^{44}_{\mathrm{ij}}m_{\mathrm{i}}m_{\mathrm{j}}}{\left(n_{\mathrm{i}\downarrow}-1\right)\left(n_{\mathrm{i}\uparrow}-1\right)\left(n_{\mathrm{j}\downarrow}-1\right)\left(n_{\mathrm{j}\uparrow}-1\right)} - \frac{I^{2}_{\mathrm{i}\downarrow}\left(m_{\mathrm{i}}+1\right)m_{\mathrm{j}}}{4\left(1-n_{\mathrm{i}\downarrow}\right)} + \frac{I^{\mathrm{j}}_{4}m_{\mathrm{i}}m_{\mathrm{j}}}{2\left(1-n_{\mathrm{j}\downarrow}\right)\left(1-n_{\mathrm{j}\uparrow}\right)}$$
$$+ \frac{I^{\mathrm{i}}_{4}m_{\mathrm{i}}m_{\mathrm{j}}}{2\left(1-n_{\mathrm{i}\downarrow}\right)\left(1-n_{\mathrm{i}\uparrow}\right)}. \tag{B.2}$$

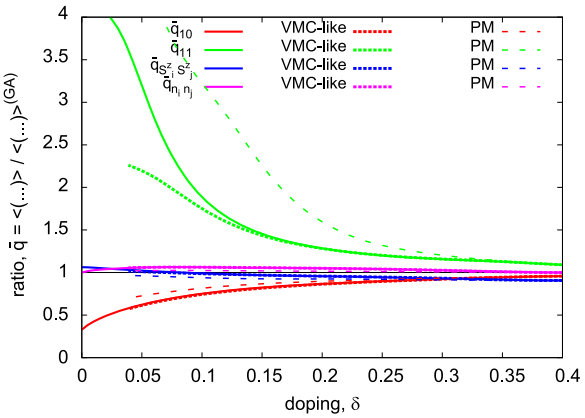

Figure C1. The ratio of the average $\left\langle \left(\ldots\right) \right\rangle_G$ obtained in the (VMC-like) DE-GWF approach with respect to that obtained in the GA.

Appendix C. Gutzwiller approximation: accuracy of the Gutzwiller factors

In figure C1 we plot the ratios of the averages $\left\langle \left(\ldots\right) \right\rangle_G$ obtained accurately within the (VMC-like) DE-GWF approach (equations (29)–(32)) and those obtained within the GA (equations (38)–(40)). Since in the GA these averages are expressed via Gutzwiller factors (e.g. g_t for the kinetic energy), the plotted ratios can serve to assess the accuracy of such Gutzwiller factors. Explicitly, we plot the following quantities:

$$\bar{q}_{\mathbf{ij}} \equiv \frac{\left\langle \hat{c}^{\dagger}_{\mathbf{i},\sigma}\hat{c}_{\mathbf{j},\sigma} \right\rangle_G}{\left\langle \hat{c}^{\dagger}_{\mathbf{i},\sigma}\hat{c}_{\mathbf{j},\sigma} \right\rangle_G^{(GA)}} = \frac{q^2 T^{11}_{\mathbf{ij}} + 2q\alpha T^{13}_{\mathbf{ij}} + \alpha^2 T^{33}_{\mathbf{ij}}}{q^2 P_{\mathbf{ij}}}, \tag{C.1}$$

$$\bar{q}_{S^z_i S^z_j} \equiv \frac{\left\langle \hat{S}^{+}_{\mathbf{i}}\hat{S}^{-}_{\mathbf{j}} + \hat{S}^{-}_{\mathbf{i}}\hat{S}^{+}_{\mathbf{j}} \right\rangle_G}{\left\langle \hat{S}^{+}_{\mathbf{i}}\hat{S}^{-}_{\mathbf{j}} + \hat{S}^{-}_{\mathbf{i}}\hat{S}^{+}_{\mathbf{j}} \right\rangle_G^{(GA)}} = \frac{2S^{22}}{\left\langle \hat{S}^{+}_{\mathbf{i}}\hat{S}^{-}_{\mathbf{j}} + \hat{S}^{-}_{\mathbf{i}}\hat{S}^{+}_{\mathbf{j}} \right\rangle_0} = \frac{S^{22}}{S^{22}(0)}, \tag{C.2}$$

$$\bar{q}_{n_i n_j} \equiv \frac{\left\langle \hat{n}_{\mathbf{i}}\hat{n}_{\mathbf{j}} \right\rangle_G}{\left\langle \hat{n}_{\mathbf{i}}\hat{n}_{\mathbf{j}} \right\rangle_G^{(GA)}} = \frac{n^2 + I^{22\uparrow\uparrow}\gamma + I^{22\uparrow\downarrow}\gamma + \left(\ldots\right)}{n^2 + I^{22\uparrow\uparrow}(0)\gamma + I^{22\uparrow\downarrow}(0)\gamma}. \tag{C.3}$$

where $\gamma \equiv \frac{(1-2n)^2}{2(n-1)^2}$, by e.g. $S^{22}\left(0\right)$ we understand the zeroth-order diagrammatic sum, and by $\left(\ldots\right)$ we denote other diagrammatic sum terms (see equation (32)). According to the above expressions, a situation in which the GA approximates the average accurately corresponds to $\bar{q} = 1$. If an average is overestimated (underestimated) by the GA, this yields $\bar{q} < 1$ ($\bar{q} > 1$). It can be seen from figure C1 that for the exchange term averages $\bar{q} \approx 1$, and therefore the GA works quite well for them. However, for the kinetic energy term averages the GA greatly overestimates the n.n. average (as also reported in [15]) and underestimates the next-n.n. average, especially for an underdoped system. This is the reason behind the large discrepancy of the GA and VMC results in this regime. The ratios $\bar{q}$ are quite similar in the VMC-like and full

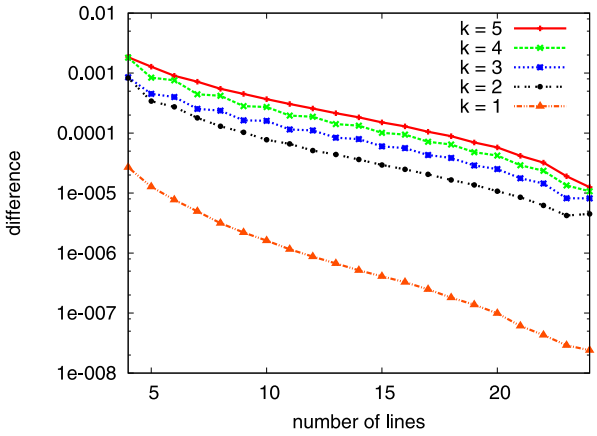

Figure D1. Convergence of the results for $\left\langle \hat{S}_{\mathbf{i}}^{z}\hat{S}_{\mathbf{j}}^{z}\right\rangle$ as a function of number of $\left|\Psi_0\right\rangle$ lines.

DE-GWF methods. They are also similar in the PM phase (however, for the next-n.n. hopping the ratio $\bar{q}_{11}$ is substantially larger).

Appendix D. Convergence analysis: number of lines

To analyze the effect of the number of $\left|\Psi_0\right\rangle$ lines included in the calculations we present in figure D1 the difference (integrated over doping values) between the correlation function $\left\langle \hat{S}_{\mathbf{i}}^{z}\hat{S}_{\mathbf{j}}^{z}\right\rangle$ for a given number of lines n and for 25 lines as a function of n.

The nearly linear behavior of the differences in figure D1 suggests that the convergence is exponential (a logarithmic scale is used in figure D1). Note also that the higher-order results converge more slowly than the lower-order results, which indicates that to obtain the same accuracy (with respect to the complete $\left|\Psi_0\right\rangle$ results with all lines included) in a higher order we need to take into account more lines than in a lower order. Therefore, not only the inclusion of higher-order terms is important to improve accuracy, but also the inclusion of longer range lines.

Appendix E. Details of the VMC-like DE-GWF calculations

We set all parameters of the effective Hamiltonian to zero, except for n.n. pairing $\Delta_{10}^{\mathrm{eff}}$ and hoppings t_{10}^{eff}, t_{11}^{eff}, as well as t_{00}^{eff}, playing the role of effective chemical potential. The n.n. hopping is kept fixed, whereas the other parameters are optimized variationally. In the resulting scheme the effective Hamiltonian contains the same variational parameters as that used in the VMC approach [9].

We have taken as nonzero the $\left|\Psi_0\right\rangle$ lines ($S_{\mathbf{i},\mathbf{j}} \equiv S_{0,(\mathbf{i}-\mathbf{j})} \equiv S_{XY}$ with $X = \left(i_1 - j_1\right)$, $Y = \left(i_2 - j_2\right)$, P_{XY}–analogously) fulfilling $X^2 + Y^2 \leqslant 25$. In the situation when the number of $\left|\Psi_0\right\rangle$ lines does not match the number of effective parameters ($t_{\mathbf{i},\mathbf{j}}^{\mathrm{eff}}$ and $\Delta_{\mathbf{i},\mathbf{j}}^{\mathrm{eff}}$), the self-consistency loop would not find the true minimum of the energy and a more standard

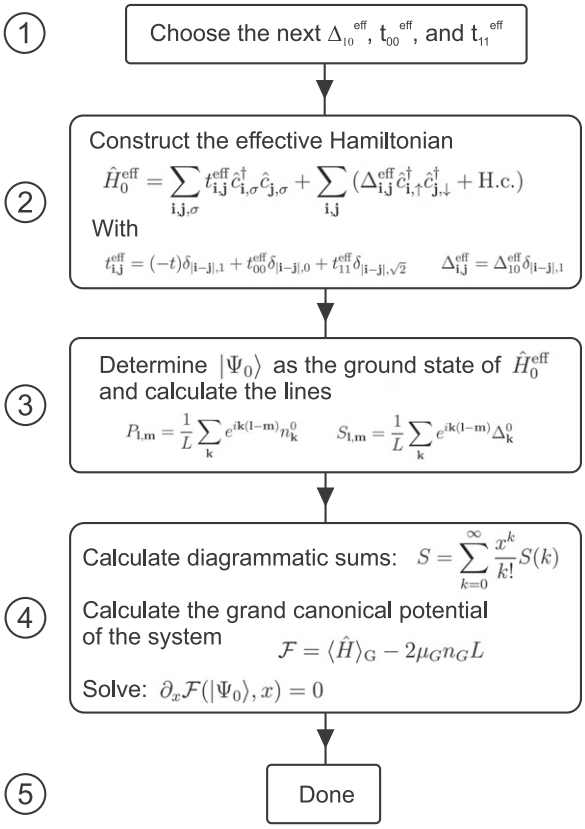

Figure E1. Flowchart of the VMC-like DE-GWF calculations.

minimization of the energy with respect to Δ_{10}^{eff}, t_{00}^{eff}, and t_{11}^{eff} is necessary. Namely, we numerically search for a minimum of the system grand canonical potential $\mathcal{F}$ by calculating its value for fixed Δ_{10}^{eff}, t_{00}^{eff}, and t_{11}^{eff}. The flowchart of such calculations is presented in figure E1. Explicitly, having fixed effective parameters (step 1 in figure E1) we may construct the effective Hamiltonian (step 2), calculate the $|\Psi_0\rangle$ lines (step 3), and having them we can obtain the diagrammatic sums and the potential $\mathcal{F}$ (step 4). Finally, we choose the solution with Δ_{10}^{eff}, t_{00}^{eff}, and t_{11}^{eff} corresponding to the lowest potential $\mathcal{F}$.

References

[1] Abram M, Kaczmarczyk J, Jędrak J and Spałek J 2013 *d*-wave superconductivity and its coexistence with antiferromagnetism in the *t-J-U* model: statistically consistent Gutzwiller approach *Phys. Rev.* B **88** 094502
[2] Anderson P W 2007 Is there glue in cuprate superconductors? *Science* **317** 1705
[3] Anderson P W 1988 *Frontiers and Borderlines in Many-Particle Physics* (Amsterdam: North-Holland)
[4] Baeriswyl D 2000 Variational scheme for the Mott transition *Found. Phys.* **30** 2033–48
[5] Bünemann J, Schickling T and Gebhard F 2012 Variational study of Fermi surface deformations in Hubbard models *Europhys. Lett.* **98** 27006

[6] Chou C-P and Lee T-K 2012 Inhomogeneous state of the extended *t-J* model on a square lattice: a variational Monte Carlo and Gutzwiller approximation study *Phys. Rev.* B **85** 104511
[7] Civelli M, Capone M, Georges A, Haule K, Parcollet O, Stanescu T D and Kotliar G 2008 Nodal-antinodal dichotomy and the two gaps of a superconducting doped Mott insulator *Phys. Rev. Lett.* **100** 046402
[8] Edegger B, Muthukumar V N, Gros C and Anderson P W 2006 Electronic structure of strongly correlated *d*-wave superconductors *Phys. Rev. Lett.* **96** 207002
[9] Edegger B, Muthukumar V N and Gros C 2006 Spontaneous breaking of the Fermi-surface symmetry in the *t-J* model: a numerical study *Phys. Rev.* B **74** 165109
[10] Edegger B, Muthukumar V N and Gros C 2007 Gutzwiller–RVB theory of high-temperature superconductivity: results from renormalized mean-field theory and variational Monte Carlo calculations *Adv. Phys.* **56** 927
[11] Efetov K B, Meier H and Pepin C 2013 Pseudogap state near a quantum critical point *Nature Phys.* **9** 442–6
[12] Eichenberger D and Baeriswyl D 2007 Superconductivity and antiferromagnetism in the two-dimensional Hubbard model: a variational study *Phys. Rev.* B **76** 180504
[13] Feng S, Zhao H and Huang Z 2012 Two gaps with one energy scale in cuprate superconductors *Phys. Rev.* B **85** 054509
[14] Fetter A L and Walecka J D 2003 *Quantum Theory of Many-Particle Systems* (New York: Dover Publications)
[15] Fukushima N 2008 Grand canonical Gutzwiller approximation for magnetic inhomogeneous systems *Phys. Rev.* B **78** 115105
[16] Fukushima N 2011 Renormalization of transition matrix elements of particle number operators due to strong electron correlation *J. Phys. A: Math. Theor.* **44** 075002
[17] Gebhard F and Vollhardt D 1988 Correlation functions for interacting fermions in the Gutzwiller ansatz *Phys. Rev.* B **38** 6911–27
[18] Gebhard F 1990 Gutzwiller correlated wave functions in finite dimensions *d*: A systematic expansion in 1/*d* *Phys. Rev.* B **41** 9452
[19] Gutzwiller M C 1963 Effect of correlation on the ferromagnetism of transition metals *Phys. Rev. Lett.* **10** 159–62
Gutzwiller M C 1965 Correlation of electrons in a narrow *s*-band *Phys. Rev.* **137** A1726
[20] Halboth C J and Metzner W 2000 *d*-wave superconductivity and Pomeranchuk instability in the two-dimensional Hubbard model *Phys. Rev. Lett.* **85** 5162–5
[21] Hanke W, Kiesel M L, Aichhorn M, Brehm S and Arrigoni E 2010 The 3-band Hubbard-model versus the 1-band model for the high-T_c cuprates: pairing dynamics, superconductivity and the ground-state phase diagram *Eur. Phys. J. Special Topics* **188** 15
[22] Hetényi B 2010 Approximate solution of variational wave functions for strongly correlated systems: description of bound excitons in metals and insulators *Phys. Rev.* B **82** 115104
[23] Howczak O, Kaczmarczyk J and Spałek J 2013 Pairing by Kondo interaction and magnetic phases in the Anderson–Kondo lattice model: statistically consistent renormalized mean-field theory *Phys. Status Solidi (b)* **250** 609–14
[24] Ivanov D A 2004 Antiferromagnetism and phase separation in the *t-J* model at low doping: a variational study *Phys. Rev.* B **70** 104503
[25] Jędrak J and Spałek J 2010 Consistent statistical treatment of the renormalized mean-field *t-J* model *Phys. Rev.* B **81** 073108
[26] Jędrak J and Spałek J 2011 Renormalized mean-field *t-J* model of high-T_c superconductivity: comparison to experiment *Phys. Rev.* B **83** 104512
[27] Johnston S, Vishik I M, Lee W S, Schmitt F, Uchida S, Fujita K, Ishida S, Nagaosa N, Shen Z X and Devereaux T P 2012 Evidence for the importance of extended Coulomb interactions and forward scattering in cuprate superconductors *Phys. Rev. Lett.* **108** 166404

[28] Kaczmarczyk J, Spałek J, Schickling T and Bünemann J 2013 Superconductivity in the two-dimensional Hubbard model: Gutzwiller wave function solution *Phys. Rev.* B **88** 115127
[29] Kaczmarczyk J and Spałek J 2011 Coexistence of antiferromagnetism and superconductivity within *t-J* model with strong correlations and nonzero spin polarization *Phys. Rev.* B **84** 125140
[30] Kądzielawa A P, Spałek J, Kurzyk J and Wójcik W 2013 Extended Hubbard model with renormalized Wannier wave functions in the correlated state III *Eur. Phys. J.* B **86** 252
[31] Khasanov R, Kondo T, Strässle S, Heron D O G, Kaminski A, Keller H, Lee S L and Takeuchi T 2008 Evidence for a competition between the superconducting state and the pseudogap state of $BiPb_2SrLa_2CuO_{6+\delta}$ from muon spin rotation experiments *Phys. Rev. Lett.* **101** 227002
[32] Kondo T, Hamaya Y, Palczewski A D, Takeuchi T, Wen J S, Gu G, Schmalian J and Kaminski A 2010 Disentangling Cooper-pair formation above the transition temperature from the pseudogap state in the cuprates *Nature Phys.* **7** 21–25
[33] Kondo T, Khasanov R, Takeuchi T, Schmalian J and Kaminski A 2009 Competition between the pseudogap and superconductivity in the high-T_c copper oxides *Nature* **457** 296–300
[34] Ko W-H, Nave C P and Lee P A 2007 Extended Gutzwiller approximation for inhomogeneous systems *Phys. Rev.* B **76** 245113
[35] Kurzyk J, Spałek J and Wójcik J 2007 Lieb–Wu solution, Gutzwiller-wave-function, and Gutzwiller-ansatz approximation with adjustable single-particle wave function for the Hubbard chain *Acta Phys. Polon.* A **111** 603
[36] Kyung B, Sénéchal D and Tremblay A-M S 2009 Pairing dynamics in strongly correlated superconductivity *Phys. Rev.* B **80** 205109
[37] Lee P A, Nagaosa N and Wen X-G 2006 Doping a Mott insulator: physics of high-temperature superconductivity *Rev. Mod. Phys.* **78** 17–85
[38] Lee W S, Vishik I M, Tanaka K, Lu D H, Sasagawa T, Nagaosa N, Devereaux T P, Hussain Z and Shen Z-X 2007 Abrupt onset of a second energy gap at the superconducting transition of underdoped Bi2212 *Nature* **450** 81–84
[39] Maier T A, Jarrell M S and Scalapino D J 2006 Structure of the pairing interaction in the two-dimensional Hubbard model *Phys. Rev. Lett.* **96** 047005
[40] Yang K-Y, Chen W Q, Rice T M, Sigrist M and Zhang F-C 2009 Nature of stripes in the generalized *t-J* model applied to the cuprate superconductors *New J. Phys.* **11** 055053
[41] Bünemann J, Gebhard F and Thul R 2003 Landau–Gutzwiller quasiparticles *Phys. Rev.* B **67** 075103
[42] Mesot J *et al* 1999 Superconducting gap anisotropy and quasiparticle interactions: a doping dependent photoemission study *Phys. Rev. Lett.* **83** 840–3
[43] Watanabe T, Yokoyama H, Shigeta K and Ogata M 2009 Momentum dependence of pseudo-gap and superconducting gap in variation theory *New J. Phys.* **11** 075011
[44] Metzner W and Vollhardt D 1988 Analytic calculation of ground-state properties of correlated fermions with the Gutzwiller wave function *Phys. Rev.* B **37** 7382–99
[45] Monthoux P, Balatsky A V and Pines D 1991 Toward a theory of high-temperature superconductivity in the antiferromagnetically correlated cuprate oxides *Phys. Rev. Lett.* **67** 3448–51
[46] Ogata M and Himeda A 2003 Superconductivity and antiferromagnetism in an extended Gutzwiller approximation for *t-J* model: effect of double-occupancy exclusion *J. Phys. Soc. Japan* **72** 374–91
[47] Ogata M and Fukuyama H 2008 The *t–J* model for the oxide high-T_c superconductors *Rep. Prog. Phys.* **71** 036501
[48] Paramekanti A, Randeria M and Trivedi N 2001 Projected wave functions and high temperature superconductivity *Phys. Rev. Lett.* **87** 217002
[49] Paramekanti A, Randeria M and Trivedi N 2004 High-T_c superconductors: a variational theory of the superconducting state *Phys. Rev.* B **70** 054504
[50] Raczkowski M, Capello M, Poilblanc D, Frésard R and Oleś A M 2007 Unidirectional *d*-wave superconducting domains in the two-dimensional *t-J* model *Phys. Rev.* B **76** 140505

[51] Randeria M, Paramekanti A and Trivedi N 2004 Nodal quasiparticle dispersion in strongly correlated *d*-wave superconductors *Phys. Rev.* B **69** 144509

[52] Sacuto A, Benhabib S, Gallais Y, Blanc S, Cazayous M, Masson M-A, Wen J S, Xu Z J and Gu G D 2013 Pseusogap in cuprates by electronic Raman scattering *J. Phys.: Conf. Ser.* **449** 012011

[53] Scalapino D J 2012 A common thread: the pairing interaction for unconventional superconductors *Rev. Mod. Phys.* **84** 1383–417

[54] Shekhter A, Ramshaw B J, Liang R, Hardy W N, Bonn D A, Balakirev F F, McDonald R D, Betts J B, Riggs S C and Migliori A 2013 Bounding the pseudogap with a line of phase transitions in $YBa_2Cu_3O_{6+\delta}$ *Nature* **498** 75–75

[55] Campuzano J C *et al* 1999 Electronic spectra and their relation to the (π, π) collective mode in high-T_c superconductors *Phys. Rev. Lett.* **83** 3709

[56] Spałek J and Goc-Jagło D 2012 On the strongly correlated quantum matter paradigm: magnetism–superconductivity redux *Phys. Scr.* **86** 048301

[57] Spałek J and Zegrodnik M 2013 Spin-triplet paired state induced by Hunds rule coupling and correlations: a fully statistically consistent Gutzwiller approach *J. Phys.: Condens. Matter* **25** 435601

[58] Spałek J 1988 Effect of pair hopping and magnitude of intra-atomic interaction on exchange-mediated superconductivity *Phys. Rev.* B **37** 533–6

Spałek J 1988 Microscopic model of hybrid pairing: a common approach to heavy-fermion and high-T_c superconductivity *Phys. Rev.* B **38** 208

[59] Spałek J unpublished

[60] Vishik I M *et al* 2012 Phase competition in trisected superconducting dome *Proc. Natl Acad. Sci. USA* **109** 18332–7

[61] Vishik I M, Lee W S, He R-H, Hashimoto M, Hussain Z, Devereaux T P and Shen Z-X 2010 ARPES studies of cuprate fermiology: superconductivity, pseudogap and quasiparticle dynamics *New J. Phys.* **12** 105008

[62] Vishik I M *et al* 2010 Doping-dependent nodal Fermi velocity of the high-temperature superconductor $Bi_2Sr_2CaCu_2O_{8+\delta}$ revealed using high-resolution angle-resolved photoemission spectroscopy *Phys. Rev. Lett.* **104** 207002

[63] Wang Q-H, Wang Z D, Chen Y and Zhang F C 2006 Unrestricted renormalized mean field theory of strongly correlated electron systems *Phys. Rev.* B **73** 092507

[64] Wysokiński M M and Spałek J 2014 Properties of an almost localized Fermi liquid in an applied magnetic field revisited: a statistically consistent Gutzwiller approach *J. Phys.: Condens. Matter* **26** 055601

[65] Yamase H and Kohno H 2000 Instability toward formation of quasi-one-dimensional Fermi surface in two-dimensional *t-J* model *J. Phys. Soc. Japan* **69** 2151–7

Yamase H and Kohno H 2000 Possible quasi-one-dimensional Fermi surface $La_{2-x}Sr_xCuO_4$ *J. Phys. Soc. Japan* **69** 332

[66] Yokoyama H, Ogata M, Tanaka Y, Kobayashi K and Tsuchiura H 2013 Crossover between BCS superconductor and doped Mott insulator of *d*-wave pairing state in two-dimensional Hubbard model *J. Phys. Soc. Japan* **82** 014707

[67] Yokoyama H, Tanaka Y, Ogata M and Tsuchiura H 2004 Crossover of superconducting properties and kinetic-energy gain in two-dimensional Hubbard model *J. Phys. Soc. Japan* **73** 1119–22

[68] Yoshida T, Hashimoto M, Vishik I M, Shen Z-X and Fujimori A 2012 Pseudogap, superconducting gap, and Fermi arc in high-T_c cuprates revealed by angle-resolved photoemission spectroscopy *J. Phys. Soc. Japan* **81** 011006

[69] Yunoki S, Dagotto E and Sorella S 2005 Role of strong correlation in the recent angle-resolved photoemission spectroscopy experiments on cuprate superconductors *Phys. Rev. Lett.* **94** 037001

[70] Zegrodnik M, Bünemann J and Spałek J 2014 Even-parity spin-triplet pairing by purely repulsive interactions for orbitally degenerate correlated fermions *New J. Phys.* **16** 033001

[71] Zegrodnik M, Spałek J and Bünemann J 2013 Coexistence of spin-triplet superconductivity with magnetism within a single mechanism for orbitally degenerate correlated electrons: statistically consistent Gutzwiller approximation *New J. Phys.* **15** 073050

[72] Zhang F C, Gros C, Rice T M and Shiba H 1988 A renormalised Hamiltonian approach to a resonant valence bond wavefunction *Supercond. Sci. Technol.* **1** 36

[73] Zhang F C and Rice T M 1988 Effective Hamiltonian for the superconducting Cu oxides *Phys. Rev.* B **37** 3759–61

Zhang F C and Rice T M Validity of the *t-J* model *Phys. Rev.* B **41** 7243

[74] Zheng X-J, Huang Z-B and Zou L-J 2014 Spontaneous Fermi surface deformation in the three-band Hubbard model: A variational Monte Carlo study *J. Phys. Soc. Japan* **83** 024705

[75] Zhou X-J *et al* 2003 High-temperature sperconductors: universal nodal Fermi velocity *Nature* **423** 398

[76] Gros C, Edegger B, Muthukumar V N and Anderson P W 2006 Determining the underlying Fermi surface of strongly correlated superconductors *Proc. Natl Acad. Sci* **103** 14298

[77] Spałek J and Oleś A M 1977 Ferromagnetism in narrow *s*-band with inclusion of intersite correlations *Physica* **86–88B** 375

[78] Chao K A, Spałek J and Oleś A M 1977 Kinetic exchange interaction in a narrow S-band *J. Phys. C: Solid State Phys.* **10** L271

[79] Spałek J 2012 Theory of unconventional superconductivity in strongly correlated systems: real space pairing and statistically consistent mean-field theory-in perspective *Acta. Phys. Polon.* A **121** 764

[80] Kaczmarczyk J 2014 Comparison of two approaches for the treatment of Gutzwiller variational wave functions arXiv:1401.6784